Wawrzenitz [Hoymann], N., Romer, R. L., Grasemann, B., Morales, L. (2019): Pre-UHP titanite archives pro- and retrograde episodes of fluid-marble-interaction (Dabie Shan UHP unit, China). - *Lithos*, *350-351*.

DOI: http://doi.org/10.1016/j.lithos.2019.105232

Note:

This is a pre-copyedited, author-produced version of an article accepted for publication in LITHOS following peer review. The version of record [Wawrzenitz, N., Romer, R.L., Grasemann, B., Morales, L.G. (2019). Pre-UHP titanite archives pro- and retrograde episodes of fluid-marble-interaction (Dabie Shan UHP unit, China] is available online at DOI: https://doi.org/10.1016/j.lithos.2019.105232

Pre-UHP titanite archives pro- and retrograde episodes of fluid-marble-interaction (Dabie Shan UHP unit, China)

N. Wawrzenitz [(*, a)], R.L. Romer [(a)], B. Grasemann [(b)], and L.G. Morales [(c)]

(a) Helmholtz Centre Potsdam German Research Centre for Geosciences, Telegrafenberg, D-14437 Potsdam, Germany, (b) Department for Geodynamics and Sedimentology, University of Vienna, Althanstrasse 14, A-1090 Vienna, Austria, (c) Scientific Center for Optical and Electron Microscopy, ETH Zürich, Switzerland

*corresponding author at: Helmholtz Centre Potsdam German Research Centre for Geosciences, Telegrafenberg, D-14437 Potsdam, Germany, Tel. +49 331 2881977

E-Mail adress: hoymann@gfz-potsdam.de (N. Wawrzenitz [Hoymann])

Highlights

- Multiple episodes of metasomatism are erased in marble but archived in titanite.
- Pre-UHP vein-filling titanite entraps original $^{87}Sr/^{86}Sr$ signature of carbonate units.
- Aqueous fluids metasomatosed marble at different depths and times.

- Metamorphic carbonates and silicates in marble show typical mantle $^{87}Sr/^{86}Sr$.
- Deformation was not a controlling factor during pervasive fluid-marble interaction.

Abstract

Deeply subducted crustal carbonate rocks are major transporters of carbon into the asthenosphere. However, mechanism and extent of the interaction of carbonate rocks at mantle depth with external fluids remain unclear. Carbonate interaction with external aqueous fluids derived from silicate rocks is of particular importance, because the associated decarbonation and dissolution reactions (i) influence the input into the subduction carbon cycle, (ii) influence rheology, and (iii) control isotope fingerprints of the interacting rocks, including the mantle. We investigate meta-carbonate rocks from the Dabie UHP unit, where marbles within a several km^2 exposure show $^{87}Sr/^{86}Sr$ isotope signatures as low as 0.7037, which are unusual for crustal carbonates, but typical for mantle rocks. We focus on a sample with a large pre-UHP titanite, crystallized in a vein, with crustal $^{87}Sr/^{86}Sr$ signatures ($^{87}Sr/^{86}Sr_i$: 0.7071-0.7075) and its fluid-mediated replacement. The titanite survived subduction to mantle depth and was altered only at its margins during subduction and exhumation. This fluid-mediated replacement is characterized by (i) very low, mantle-like $^{87}Sr/^{86}Sr$ signatures (as low as 0.7045), both in the titanite reaction rim and the marble matrix, and (ii) significantly higher $^{87}Sr/^{86}Sr$ signatures (ca. 0.7085) related to allanite replacing titanite along discrete veins during retrogression.

Combining mineral-scale Sr-isotope analyses with microfabric and mineral-chemical data of titanite, white mica, and calcite, allows for establishing five episodes (A to E) of fluid-mineral interaction linked with the pro- and retrograde reaction history: (A) prograde episode of interaction with aqueous fluid sourced from dehydration reactions in the impure marble or

from subducting crustal rocks; titanite crystallized from fluid in a vein and acted as a sink for Ti, REE and Sr from the protolith, (B) fluid-interaction resulted in the replacement of titanite by rutile in the rim of the prograde titanite, ductile deformation lead to shape-preferred orientation of mineral relicts of the HP-UHP stage, (C) infiltration of a mantle-derived fluid is recorded by the back – reaction to titanite, whose $^{87}Sr/^{86}Sr$ signatures reflect mixing between the fluid from dissolved prograde titanite and the incoming fluid, (D) the continued interaction of the mantle-derived fluid with the marble resulted in pervasive replacement and mantle-like $^{87}Sr/^{86}Sr$ signatures of the minerals in the matrix, and (E) infiltration of a fluid sourced from crustal rocks or from metasomatized mantle fragments along grain boundaries and fractures at the retrograde episode E related to emplacement in the middle crust. We show that dissolution-precipitation reactions efficiently supported material transport and isotope chemical exchange between titanite and its meta-carbonate host rock, depicting Sr isotope mixing associated with dissolution and precipitation. Deformation was not a controlling factor. The fluid-mineral interaction episodes are related to map-scale metasomatism and the change of the isotope fingerprint of the marbles.

Keywords: fluid-rock-interaction; Sr isotopes; micro-drilling; mantle fluid; titanite-rutile reaction; dissolution-precipitation

1. Introduction

Understanding the degree of interaction of aqueous fluids with carbonate rocks in subduction zones is particularly important for comprehending the deep carbon cycle. Carbonate rocks are the major transporters of carbon into the upper mantle, where metasomatism may transfer a

78 significant amount of carbon to the mantle wedge and into the convecting mantle. Infiltration
79 of aqueous fluids is associated with decarbonation and dissolution reactions having an
80 important effect on the CO_2 budget in subduction zones (Manning, 2014; Ague and Nicolesu,
81 2014). Extent, mechanisms, timing and pathways of infiltration of aqueous fluids into
82 carbonate rocks during subduction and exhumation, however, are still controversially debated
83 (e.g. Frezotti et al., 2011).

84 Wang and Rumble (1999), Rumble et al. (2003), Zheng et al. (2007), Liou et al. (2012), and
85 Zhang et al. (2011) investigated crustal carbonate rocks in the Dabie and Sulu UHP units,
86 originally formed in the Neoproterozoic (Rumble et al., 2000; Prave et al., 2018) and
87 metamorphosed at UHP conditions during Triassic continental collision. They suggested
88 minor internally buffered fluid-mineral interaction, and only insignificant infiltration of
89 aqueous fluids and metasomatism in the deep subduction zone, until retrogression. In contrast,
90 Romer et al. (2003) showed that aqueous fluids infiltrated carbonate rocks of the Dabie UHP
91 unit during subduction to mantle depths. This idea was increasingly taken up by later studies
92 of deeply subducted carbonate rocks in the Dabie and elsewhere (Ohta et al., 2003; Frezzotti
93 et al., 2011, 2015; Ogasawara, 2014; Ague and Nicolescu, 2014; Wang et al., 2014; Liu et al.,
94 2015; Liu et al., 2017; Ferrando et al., 2017; Tao et al., 2018). In line with Romer et al.
95 (2003), Wang et al. (2014) suggested a complete alteration/change of protolith signatures
96 through fluid-mediated reactions, along the subduction zone, based on O and Mg isotope
97 whole rock analyses of marbles and enclosed eclogites (Sulu UHP unit). Liu et al. (2017)
98 suggest metasomatism during early exhumation by fluids originating from previously
99 subducted oceanic crust.

100 The mantle-like $^{87}Sr/^{86}Sr$ values below 0.7045 recorded in the Dabie UHP marbles (Romer et
101 al., 2003) are too low for late Neoproterozoic marine carbonate protoliths that are expected to
102 have $^{87}Sr/^{86}Sr$ values between 0.7070 and 0.7076 (Veizer et al., 1999; Prokoph et al. 2008).

103 The mantle-like $^{87}Sr/^{86}Sr$ values are clearly indicative for the interaction of the marble with
104 MORB- and/or mantle derived fluids ($^{87}Sr/^{86}Sr$ values below 0.7045, White 2010). Based on
105 Sr isotope investigations of marbles from the Changpu complex (Dabie UHP unit; Fig. 1 a),
106 combined with petrological and geochemical investigations, Romer et al. (2003) inferred that
107 interaction of aqueous fluids with crustal carbonates occurred along the subduction zone. In
108 accordance with this, the modelled XCO_2 at peak PT conditions in these rocks has been very
109 low (Romer et al., 2003), as recently confirmed by Liu et al. (2015) for marbles from the
110 Dabie UHP unit. From geochemical results, showing that carbonates from the purest marbles
111 have the least radiogenic Sr isotopic composition and the highest Sr concentration (Fig. 1 b),
112 Romer et al. (2003) interpreted, that the fluid infiltration was paralleled by the introduction of
113 Mg and less radiogenic Sr and the loss of Si, K, and Na. The marbles of the Dabie UHP unit
114 clearly record infiltration of aqueous mantle-derived fluids that metasomatized carbonates
115 within a several km^2 marble exposure (Romer et al., 2003). The Sr isotopic composition of the
116 fluid source is most readily reflected by the marbles having the least radiogenic composition.
117 More radiogenic Sr values in the marbles may relate to incomplete replacement processes and
118 mixing between fluid from dissolved carbonate and the incoming mantle-derived fluid. Thus,
119 these marbles potentially provide insight into the fluid-rock interaction history and associated
120 transport and replacement mechanisms.

121 The mechanisms of fluid transport accounting for the observed loss of the original Sr isotopic
122 fingerprint in the purest UHP marbles were not explained by Romer et al. (2003). This is
123 mainly because the Sr isotope analyses were performed on bulk calcium carbonate fractions
124 from hand specimen. The whole rock data do not allow for (i) linking the results to the fluid-
125 mineral reaction history and (ii) detecting multiple fluid-rock interaction processes.
126 Furthermore, they do not allow for identifying, whether and how ductile deformation, discrete

127 pathways or pervasive dissolution-precipitation processes (e.g. Putnis and Austrheim, 2010)
128 were responsible for the infiltration of fluids from an external source.

129 Sr isotopic compositions determined on the mineral-scale are particularly suited to detect fluid
130 interaction processes in carbonate and calcsilicate rocks, as the constituting minerals such as
131 calcite, dolomite, diopside, clinozoisite, titanite, and allanite are almost free of Rb, precluding
132 reaction-induced isotopic heterogeneity to be masked by in-situ ^{87}Sr growth. Titanite is
133 capable of recording successive episodes of the fluid-rock interaction history and its $^{87}Sr/^{86}Sr$
134 ratio may be a sensitive tracer for successive fluid-mineral-interaction processes (Lucassen et
135 al., 2011).

136 The Sr isotopic compositions of Neoproterozoic marine carbonates, of mantle/MORB, of
137 gneisses from Dabie Shan ($^{87}Sr/^{86}Sr$ values above 0.7080, Ma et al., 2000), and of the
138 interacting fluids are distinct from each other. This allows for identifying fluid-mineral
139 reactions and for resolving distinct fluid sources and interaction episodes.
140 Sr isotopic compositions on the mineral-scale allow for identifying fluid pathways that may
141 be pervasive through the rock volume by dissolution-precipitation replacement (Putnis and
142 Austrheim, 2010) or channelized along veins (Oliver and Bons, 2001). Fluid flow may occur
143 along grain boundaries and tectonic fractures (e.g. Fein et al., 1994; Holness & Graham,
144 1995) that may form an interconnected network, which provides channelized pathways for
145 both externally and internally derived fluids and, thus, represent an open system. Moreover,
146 dissolution-precipitation processes are important for creating fluid pathways by replacement
147 and fracturing (Putnis, 2002, 2009; Jamtveit et al., 2009; Wawrzenitz et al., 2012). In contrast
148 to tectonic fractures, hydrofractures that are the result of increased fluid pore pressure
149 (Jamtveit et al., 2009), commonly do not form an interconnected network that would allow
150 infiltration of external fluids. Once they have formed, hydrofractures are sinks for (internal)
151 fluids released from the adjacent wall rock rather than pathways for external fluid.

We study in detail such a marble sample containing a pre-UHP titanite megacryst crystallized from fluids either in a tectonic fracture or in a hydrofracture (Fig. 1 c; Wawrzenitz et al., 2006). The contrasts in $^{87}Sr/^{86}Sr$ isotopic compositions of titanite core and bulk carbonate matrix (~0.7073 and ~0.7045, resp.), observed by Wawrzenitz et al. (2006), raised the expectation, that *in-situ* Sr-isotope investigations combined with mineral chemical and micro-fabric investigations on the grain-scale will give a detailed insight into the fluid-mineral interaction path in deeply subducted carbonate rocks.

With the selected sample the following hypotheses are tested:

(i) Does the Sr isotopic composition of the titanite core reflect the composition of remote external fluids? In this case, the titanite would have precipitated from external fluids channelized in a tectonic fracture.

(ii) Or does the Sr isotopic composition of the titanite core reflect the composition of the original Neoproterozoic fluids of the carbonate protolith? In this case, the titanite would have precipitated from fluids released from the immediate host rock into a propagating hydrofracture. Fluid overpressure could be the result of pervasive infiltration of external fluid through the carbonate rock.

(iii) What is the transport mechanism of fluid flow through the carbonate rocks? Did the fluid migrate along cracks and/or silicate-carbonate phase boundaries? Are coupled dissolution-precipitation replacement processes underlying the pervasive infiltration?

(iv) What is the role of crystal-plastic deformation for the transport of fluid and for chemical and isotopic changes in the titanite megacryst and the marble matrix?

(v) Did infiltration and metasomatism occur during one or several successive episodes?

(vi) How are successive episodes of infiltration linked to the mineral reaction and deformation history?

We here combine texturally controlled "in-situ" Sr isotope analysis at the crystal-scale in the titanite megacryst with mineral-chemical analysis, using microdrilling and the ID TIMS technique for achieving the required precision and accuracy. We analyze the microstructures and lattice preferred orientations (CPOs) within the titanite megacryst and the reaction rim with a SEM using the EBSD technique (Prior et al., 1999) aiming at determining crystalplastic deformation or other potential deformation mechanisms. In combination with mineral chemical analyses, EBSD mapping allows for recognizing (i) the relationships between deformation mechanisms and chemical changes of titanite during the reaction history and (ii) mechanisms of fluid-induced mineral replacement, i.e. coupled dissolution-reprecipitation vs. new crystallization, thus highlighting the role of deformation in fluid-titanite interaction.

The combination of our results has the potential to characterize the mechanisms of aqueous fluid infiltration and migration in carbonate rocks, modifying the original chemical signatures of these rocks on the km-scale.

2. Geological setting

The Qinling–Dabie–Sulu metamorphic belt (Eastern China) is the result of Triassic collision between the Yangtze craton (South China block) in the south and the Sino-Korean craton (North China block) in the north. Crustal rocks underwent UHP-metamorphism and are characterized by a long-lasting (some tens of my) complex metamorphic history of ultradeep subduction and exhumation (Hacker et al., 2004; Zheng et al., 2005, 2009; Wawrzenitz et al., 2006; Brouwer et al., 2011; Wang et al., 2012; Wu and Zheng, 2013).

The Dabie metamorphic belt consists of tectonic complexes that are characterized by a wide range of P–T conditions (Fig. 1a) and that are bound by shear zones. The following main

tectonic complexes were identified: (i) the North Dabie Complex is a high-temperature UHP unit with HT- eclogites, magmatitic gneisses as well as granulitic relics (Wang et al., 1998; Okay et al., 1989; Faure et al., 2003; Bryant et al., 2004) that locally contain UHP minerals (e.g., microdiamonds, Xu et al., 2003); (ii) the Central Dabie Complex also shows UHP relicts (microdiamonds and coesite), but is characterized by lower temperatures; (iii) the South Dabie Complex is a low-temperature unit containing amphibolitized HP rocks with UHP relics (Li et al., 2004); and blueschist-facies rocks in the south.

The investigated samples are from the Central Dabie Complex, which is mainly composed of eclogites, paragneisses, orthogneisses, marbles, quartzites, and garnet peridotites. The P-T path of these units is broadly defined by three major equilibration stages: (i) UHP conditions are evidenced by diamond, coesite and jadeite-rich inclusions in garnet; the maximum pressures are >2.8 GPa at 700–800 C (e.g., Hacker et al., 2006); (ii) a first major episode of decompression/exhumation (Liou et al., 2009; Zheng, 2008) associated with a temperature increase from ca. 700° to 780°C (Schmid et al. 2003), locally even to 800°-850°C (e.g. Liu et al., 2015) produced eclogite mineral assemblages at 1.5-2.5 GPa; and (iii) a second major episode of decompression/exhumation into the field of amphibolite facies results in the decomposition of omphacite into symplectites mainly composed of amphibole and plagioclase (Li et al., 2012).

Geochronological data of the Northern, Central and Southern Dabie complexes obtained with different methods yielded age constraints for episodes of fluid availability. For instance, U-Pb zircon SHRIMP ages of 242 ± 2 Ma and 227 ± 2 Ma of eclogite lenses within the Dabie UHP marbles, including the Changpu unit, have been interpreted by Wu et al. (2006) as stages of zircon growth during two episodes of fluid availability, i.e., at the onset of prograde transition from HP to UHP during deep subduction and at the retrograde transition from UHP to HP regimes during early exhumation. Liu et al., 2006 confirmed these episodes by Shrimp

zircon U-Pb dating from dolomitic marble and dated a younger episode at 218-206 Ma. Vein formation, indicating fluid flow at 217 ±2 Ma and 210 ±2 Ma has been recorded by Franz et al. (2001), Sheng et al. (2013), and Guo et al. (2012, 2015).

The studied calcsilicate marble sample derives from a suite of metacarbonate rocks from the Changpu Unit in the Central Dabie Complex. The metacarbonate rocks in part are characterized by mantle-like Sr isotopic compositions that reflect the infiltration of mantle-derived fluids (Fig. 1b, c; Romer et al. 2003). The marbles are tectonically juxtaposed against para- and orthogneisses and contain enclaves of amphibolites, eclogites, and peridotites. They record UHP metamorphism and are retrogressed to variable degree (Schmid et al., 2003). The UHP assemblage including omphacite, garnet, rutile, phengite, calcite (aragonite?), and quartz (coesite) is only preserved in slightly retrogressed calcsilicate rocks. Maximum PT conditions of ca. 42 kbar at 750°C are estimated based on the peak minerals garnet, omphacite, and phengite (Wang and Liou, 1993; Schmid et al., 2003, Liu et al., 2015) and imply exhumation from more than ca. 120 km depth. They are overprinted and locally intensely strained under amphibolite facies conditions at temperatures above 600°C (Liou et al., 1997).

3. Analytical techniques

Mechanical microsampling, sample dissolution, chemical separation of Rb and Sr and the ID-TIMS technique allowed resolving small $^{87}Sr/^{86}Sr$ isotope variations within the reaction rim of the titanite megacryst at the grain scale (Fig. 2a). We used Rb/Sr microsampling to obtain titanite, calcite, and allanite samples of about 0.14-0.64 mg resulting in ca. 30 ng Sr. The microsamples for the Rb/Sr study have been milled out of a 100 µm polished thick section using a New Wave Merchantek™ System at the universities of Münster and Potsdam, following the technique described in Charlier et al. (2006). Calcite has been obtained by microdrilling single grains, avoiding calcite grain boundaries that show a different

composition and texture with fewer pores. In addition, small fragments of titanite, allanite and calcite have been broken directly from the megacryst and selected under the microscope. From a small ca. 3x2x1 cm sized host rock volume bordering to the titanite megacryst, we analysed multigrain fractions of matrix titanite, clinozoisite, calcite, and amphibole. Matrix titanite was separated under the microscope in one fraction containing rutile inclusions and another fraction without rutile inclusions. A critical point in microsampling the titanite reaction rim is to avoid mixed sampling domains. Therefore, the selection of drill sites based on SEM-BSE and element distribution images as well as reflected and transmitted light microscopy. Moreover, we determined the Ca/Al and Ti/Al ratios (ICP-OES) from part of the dissolved titanite samples to detect and exclude calcite impurities possibly incorporated during microdrilling of titanite. The Al-F rich and poor domains of the titanite rim could not be drilled separately.

Chemical separation of Rb and Sr was performed using Sr specific resin in 50 µl columns following the procedure described in Pin and Bassin (1992) and Lucassen et al. (2011). Rb/Sr isotope analyses were performed at GFZ on a Triton MC TIMS (Thermo Fisher), using Re filaments and a TaF activator (modified after Birck, 1986) for Sr analyses. Rb and Sr concentrations were determined by isotope dilution, using mixed ^{87}Rb–^{84}Sr spikes. The data were corrected for isotope fractionation to $^{86}Sr/^{88}Sr=0.1194$, Strontium reference material NBS 987 yielded 0.710244 ±8 (2σ, n = 10) during this study. For comparison, McArthur et al., 2000 give a value of $^{87}Sr/^{86}Sr$ = 0.710248 ± 3 (2SE). Decay constants are those recommended by Villa et al. (2015). Standard errors of ±0.005% for $^{87}Sr/^{86}Sr$ ratios and of ±1.5% for Rb/Sr ratios, as derived from replicate analyses of spiked samples, have been applied. Analytical uncertainties are reported as $2\sigma_m$ for Sr and as 2σ for Rb. Rb/Sr analytical data are given in Table 1 and are shown in Fig. 4. Major-element compositions and element distribution maps in titanite and matrix minerals were performed with a JEOL Hyperprobe

276 electron microprobe with a WDS/EDS combined micro-analyzer at GFZ using the following
277 analytical conditions: 15 kV accelerating voltage, 20 nA beam current and 2 μm spot size.
278 The counting time varied between 10 s and 60 s for different elements. Natural and synthetic
279 oxides were used as standards, and a program on the basis of the ZAF procedure was used for
280 calibration. The back-scattered electron (BSE) images were made with the FEG ZEISS SEM
281 at GFZ.

282 Crystallographic preferred orientations (CPO) of titanite, calcite, quartz, and rutile were
283 determined via automated indexation of electron backscatter patterns (EBSD) in a scanning
284 electron microscope (Prior et al., 1999). The sample was first polished using standard
285 methods with diamond pastes of different grain sizes up to 0.25 μm. To remove any effect of
286 damage on the sample's surface we conducted a chemical-physical polishing step using a soft
287 cloth and an alkaline solution of colloidal silica for 1 hour. The EBSD measurements were
288 carried out using a FEI Quanta 3D FEG dual-beam machine equipped with an EDAX-TSL
289 Digiview IV EBSD detector and TSL software OIM 5.31, installed at GFZ. The analysis was
290 conducted on an uncoated sample under low vacuum (10 Pa of H_2O) using the following SEM
291 parameters: 15 kV accelerating voltage; 8 nA beam current; 12 mm working distance; step
292 size of 1 μm and 70° sample tilt. Post-acquisition treatment included the standardization of
293 the confidence index (CI) of different points and CI correlation between neighbour points.
294 Grain dilation were carried out in three steps considering the grain tolerance angle of 10° and
295 a minimum grain size of 10 pixels. Only data with CI>0.1 are shown here.

296

297 ## 4. Results

298 ### 4.1 Mineral record of successive metamorphic episodes

299 The investigated calcsilicate sample (Changpu unit; Dabie UHP complex; sample 9864 from
300 Wawrzenitz et al., 2006; coordinates N30°42.454/E116°15.007) is special as it contains a
301 large titanite porphyroclast (Fig. 1c and Fig. 2a) whose core has a U-Pb age of ca. 244 Ma that
302 is linked to prograde metamorphism. Mineral relicts of the UHP assemblage are phengite (Si
303 content 3.6 p.f.u.) and rutile.

304

305 ***4.1.1 Mineral record of the matrix and relation to successive metamorphic reaction***
306 ***episodes***

307 The rock matrix (Fig. 2b) mainly consists of calcite (c. 80%) and rare dolomite. The core of
308 the grains is highly porous; the pores are typically decorating cleavage planes (Fig. 3a). The
309 chemical composition of the carbonate grains varies according to their microstructural
310 position (Fig. 3b). In the calcite grains, the Mg content increases around pores. Locally,
311 dolomitic patches are aligned along cleavage planes in the calcite grains. The Sr content of
312 calcite in the matrix is significantly higher than in the reaction rim and in veins within the
313 core of the large titanite (Table 1). Pyrite locally precipitated along calcite pore walls. Allanite
314 crystallized at calcite grain boundaries.
315 Additional matrix minerals include three generations of phengite that differ in chemical
316 composition (from Si contents >3.6 p.f.u. in unzoned old grains to 3.3 p.f.u. in retrograde
317 grains), biotite, titanite (X_{Al}= 0.09-0.15, the same chemical composition as titanite III in the
318 reaction rim) with and without rutile inclusions, and symplectites of intergrown clinozoisite,
319 An-plagioclase, amphibole, and rare titanite, forming pseudomorphs after Ca-clinopyroxene
320 (diopside). The mineral assemblages, representative for the successive metamorphic reaction
321 stages are shown in Supplement S1. Several stages of decompression are recorded:

322 The oldest stage of decompression recorded by the microfabrics comprises the decomposition
323 of omphacite to Ca-clinopyroxene and albite. During this stage, titanite and phengite formed

at the expense of older high Ti-phengite, which is typical for UHP conditions (Fig. 2c). The Si content of unzoned phengite is 3.6 p.f.u.

During a later decompression stage, from HP to amphibolite facies conditions, symplectites after diopside formed (Fig. 2b). Subsequently, biotite, and titanite formed at the rim of phengite (Fig. 2c). This phengite shows a Si content of 3.3 p.f.u. at the rims, locally increasing towards 3.4 p.f.u. in the core. In both, little and strongly retrogressed marbles, an early deformation increment, probably at HP-UHP conditions is reflected by shape-preferred orientation of phengite and omphacite, which became replaced by elongated symplectites, and of rutile, now rimmed by titanite. The external foliation deflects around the titanite megacryst (Fig. 1c).

4.1.2 Titanite megacryst and its reaction rim

The titanite megacryst forms a prograde relict within the foliated calcsilicate host rock (Wawrzenitz et al., 2006) and is accordingly interpreted as titanite I (Fig. 2a). The titanite megacryst crystallized during prograde metamorphism of marine carbonate rocks. Its large size of ca. 2x3 cm is typical for a hydrothermal mineral precipitated in a vein. The core of the titanite megacryst (titanite I) shows a homogeneous chemical composition (X_{Al}= 0.18-0.19).

Only in the rim, the titanite megacryst has been altered by later reaction (Fig. 2; Supplement S1). This reaction rim formed between the titanite megacryst and the marble. It is sharply bounded against the core of the titanite (Fig. 2d). The reaction rim consists of titanite, rutile, quartz, and calcite (Figs. 2d-h). The rutile inclusions are aligned parallel to the external trace of the foliation in the marble around the titanite megaryst. Rutile formed by the reaction titanite+fluid (CO_2)→rutile+SiO_2+$CaCO_3$. Rutile could have formed as a result of PT changes during subduction or, alternatively, a change in X_{CO_2} of the fluid. Wawrzenitz et al. (2006)

interpreted rutile to have formed during prograde fluid-rock interaction based on microstructural relationships.

A back-reaction from rutile to a chemically distinct titanite is recorded by growth of titanite at the expense of rutile (Figs. 2g, h). The boundary between this titanite and the core (titanite I) is sharp. In contrast to the chemically homogeneous core, the titanite in the reaction rim is characterized by irregular compositional zoning of portions with higher (X_{Al}= 0.21-0.27, titanite II) and lower Al and F contents (X_{Al}= 0.09-0.15, titanite III) than in the core (Figs. 2d, e, f; S2; S4).

In the outer part of the rim, albite formed from the jadeite-component of omphacite during the early decompression and fluid-interaction. The relict mineral assemblage (high X_{Al} titanite II, albite, and calcite) was found only in the outer rim. Local apatite and fluorite highlight the high fluorine content of the infiltrating fluid. During a later decompression stage, allanite replaced titanite in veins of the large pre-UHP titanite (Fig. 2i-n). In addition, calcite and Fe-, CuFe-, Pb, and Sb- sulfides precipitated in these veins.

4.2 Rb-Sr isotope data

We determined the initial Sr isotopic compositions of the successive titanite and calcite generations in vein and matrix, as well as of clinozoisite, amphibole, albite, and of allanite in fractures and along grain boundaries. We sampled titanite from the core and the reaction rim and calcite and allanite from the veins by microdrilling. The results of the Rb-Sr analysis are shown in Fig. 4 and listed in Table 1.

Calcite, clinozoisite, amphibole, and small titanite grains obtained by mineral separation from the marble matrix adjacent to the titanite megacryst, have isotopically homogeneous and unusually low $^{87}Sr/^{86}Sr$ values ranging between 0.70467±1 for clinozoisite and 0.70445±1 for

372 calcite (calculated back to 240 Ma). These values are unusual for crustal carbonates, but
373 typical for mantle. Porous cores of calcite grains, microdrilled close to and distant from the
374 titanite megacryst, also show $^{87}Sr/^{86}Sr$ values of 0.70445±1 - 0.70449±1 (calculated back to
375 240 Ma). The Sr content of calcite in the matrix is significantly higher than in the reaction rim
376 and in veins within the core of the large titanite.

377 The core of the titanite megacryst shows initial $^{87}Sr/^{86}Sr$ values, ranging between 0.70705±1
378 and 0.70744±1 (calculated back to 240 Ma), consistent with previous data obtained from
379 larger sample volumes of the titanite core (Wawrzenitz et al., 2006). These values fall within
380 the range of values typical for Neoproterozoic and younger marine carbonates that are likely
381 protoliths of the Dabie carbonates (Romer et al., 2003 and references therein, Veizer et al.,
382 1999).

383 The titanite samples obtained by microdrilling the titanite reaction rim represent mixtures,
384 with Al-F rich domains dominating. All titanite rim samples fall on a two-component mixing
385 line (Fig. 4). The radiogenic $^{87}Sr/^{86}Sr$ end member composition corresponds to that of the
386 titanite core (> 0.70705). The less radiogenic $^{87}Sr/^{86}Sr$ end member composition of the mixing
387 line is c. 0.70533±1, recorded in the samples of calcite and titanite from the reaction rim. This
388 is the same $^{87}Sr/^{86}Sr$ value recorded in albite associated with the titanite reaction rim, and in a
389 calcite vein in the titanite core. This composition is significantly more radiogenic than the one
390 of the mineral phases in the matrix (calcite, clinozoisite, titanite, amphibole) showing $^{87}Sr/^{86}Sr$
391 values of 0.7045 – 0.7047.

392 A distinctly more radiogenic $^{87}Sr/^{86}Sr$ value (c. 0.7080) is recorded in allanite and a calcite
393 vein in the titanite core. There are two types of allanite, i.e., allanite that replaced titanite I
394 occurs in veins in the titanite core and allanite that precipitated along calcite grain boundaries
395 in the marble matrix. Both types of allanite show the same $^{87}Sr/^{86}Sr$ ratio (Fig. 4, Table 1).

396

397 **4.3 Microstructural record**

398 Calcite grains within the marble matrix are equant shaped lacking shape-preferred orientation,
399 and show equilibrium grain boundary configurations. The shape-preferred orientation of
400 mineral relicts of the HP-UHP stage, i.e. of phengite with Si about 3.6 p.f.u., of symplectites
401 that replaced the elongated omphacite, and of rutile (rimmed by titanite) suggest
402 crystallization during ductile deformation. Hence, this early deformation increment probably
403 relates to HP-UHP conditions.

404 The internal fabric of the symplectites and the replacement products of phengite suggest that
405 ductile deformation had ceased before recrystallization of matrix minerals. The
406 recrystallization and the subsequent episodes of fluid-rock interaction during decompression
407 were not accompanied by the ductile deformation of the matrix that formed the foliation
408 around the titanite megacryst.

409 In agreement with this, titanite and calcite within the reaction rim do not show any indications
410 of crystalplastic deformation such as subgrain boundaries and undulatory extinctions. A
411 pattern of conjugate fractures developed in the titanite megacryst, but not in the marble matrix
412 (Fig. 2a). These fractures are preferably oriented at high angle to the trace of the foliation in
413 the marble matrix. Under the microscope, they are visible as trails of secondary fluid
414 inclusions.

415

416 ***4.3.1 EBSD mapping of titanite***

417 The optically undeformed core of titanite I is generally free of subgrains that would be
418 indicated by lattice misorientations (Fig. 5a). The titanite II and III at the rim consists of (i) re-
419 or newly crystallized grains showing a variable and large degree of misorientation of the

crystal lattice with respect to the core (Fig. 5a; b) and (ii) portions that show lattice orientation identical to that of the core (Fig. 5c; d). Reaction-driven fracturing of rutile is recorded by fractures propagating from etch pits at the rutile-titanite-interface (Fig. 2g; h). Titanite II crystallized in these fractures.

(Isotope)chemical changes are not systematically related to subgrains. In our previous study, the chemical composition has been shown to be rather homogeneous along a profile across the megacryst core (Wawrzenitz et al., 2006). Only one subgrain has been observed. This subgrain is spatially related to fractures and cleavage planes, along which slip occurred (Fig. 5f). Local chemical changes in the core are spatially linked with fractures and formation of allanite (Fig. 2j; n).

5. Discussion

5.1 The successive fluid-rock interaction episodes

The different $^{87}Sr/^{86}Sr$ values in the marble matrix, titanite core, reaction rim and in late veins and along grain boundaries (allanite and calcite) correspond to successive episodes of fluid-mineral interaction. We resolved five successive fluid-rock interaction episodes (Figs. 4 and 6; Table 2). The results exemplarily illustrate that isotope data on minerals are required to resolve a multistage fluid - mineral reaction history of a rock, rather than bulk rock data.

The partly replaced titanite megacryst is a microfabric relict. It is an archive preserving the prograde and early retrograde episodes of fluid-rock interaction. Its calcsilicate matrix preserves multistage mineral replacements related to the retrograde metamorphism of the rocks. The product phases of the successive mineral reactions show several diagnostic features of fluid-mineral interaction, i.e. porosity, vugs, fractures, sharp boundaries between

chemically distinctive zones in mineral grains, and demonstrably reflect fluid-mineral interaction during all replacement episodes (Putnis, 2009).

During the dissolution-precipitation reactions, the product phases incorporate Sr from the interacting fluid and from the dissolved precursor. The varying Sr isotopic composition traces locally restricted and/or successive replacement processes. It is important to note that

(i) interaction with a reactive fluid does not necessarily relate to infiltration of external fluid. Changes in PT, deformation and mineral reaction processes (dehydration reaction, melting during subduction) may decrease the pore volume and release fluids, hence increase the fluid pressure. This may influence the composition and reactivity of the internal fluid, and mediate a new episode of interaction with the mineral phases, without infiltration of an external fluid.

(ii) variations in Sr isotopic composition among or within product phases do not necessarily reflect pulses of infiltration of new fluids introducing Sr with different isotopic composition. Small-scale heterogeneity of $^{87}Sr/^{86}Sr$ ratios may be the result of dissolution of different local sources (Romer, 2001; Wawrzenitz et al., 2015). For instance, titanite I is a local source for radiogenic Sr ($^{87}Sr/^{86}Sr \sim 0.7075$) that may shift the Sr isotopic composition of the product minerals that precipitate in the reaction rim towards more radiogenic compositions. A few mm away from titanite I, the influence of less radiogenic Sr ($^{87}Sr/^{86}Sr \sim 0.7045$) from the fluid dominates the Sr isotopic composition of the minerals that precipitate in the marble matrix. Accordingly, the Sr isotopic composition of minerals (i.e. titanite, calcite) that precipitated during one fluid-interaction episode may be locally heterogeneous. This particularly occurs when little fluid is involved and/or the Sr isotopic compositions of precursor minerals and infiltrating fluid are very different. On the other hand, a homogeneous isotopic composition among precipitated minerals indicates important fluid percolation (and Sr mixing) during dissolution-precipitation processes. The scale over which the external

fluids migrate and support homogenization mainly depends on fluid pathways and fluid composition as dissolution-precipitation processes are fast compared to diffusion-controlled processes (Putnis and Austrheim, 2010; Villa, 2006).

5.1.1 Episode A, formation of vein titanite

The titanite megagcryst formed during episode A (Table 2, Fig. 6). The shape-preferred orientation of HP/UHP mineral relicts in the matrix is deflected around the titanite megacryst (Wawrzenitz et al., 2006), which implies that this titanite I formed during the prograde PT-path preceding the HP/UHP episode (Fig. 6). The prograde formation of titanite I is consistent with its U-Pb TIMS age of 244 ±4 Ma (Wawrzenitz et al., 2006). The same age range (245-240 Ma) has been recorded by Li et al. (2004) and Wu et al. (2006) for subduction prior to the onset of peak ultrahigh-pressure metamorphism in the Dabie UHP rocks.

The Sr isotopic composition of several marble samples across the Changpu unit in Dabie Shan range from 0.7085 to 0.7037 (Romer et al., 2003). The higher $^{87}Sr/^{86}Sr$ values fall in the range typical for late Proterozoic and younger marine carbonates (~ 0.7070-0.7076, Veizer et al., 1999; Jacobsen and Kaufman, 1999). Rocks with lower $^{87}Sr/^{86}Sr$ values are characterized by higher MgO and lower SiO_2, Al_2O_3, and K_2O contents, which was interpreted to reflect fluid-mediated exchange with a low-$^{87}Sr/^{86}Sr$ reservoir (Romer et al., 2003). As the marbles had experienced UHP metamorphism, this low-$^{87}Sr/^{86}Sr$ reservoir was inferred to be the mantle (Romer et al., 2003). The Sr isotopic composition (~ 0.70711-0.70759) preserved in the core of the titanite megacryst falls in the range expected for the likely protoliths of the marbles. It contrasts to the mantle-like Sr isotopic composition of the adjacent marble matrix (~ 0.70445-0.70467) and the reaction rim of titanite I (~ 0.70705-0.70533). Therefore, the titanite megacryst formed before the matrix minerals acquired their more unradiogenic Sr. This is consistent with the observed (re)crystallization history.

494 The titanite I precipitated in a fracture from a fluid, whose Sr isotopic composition was
495 dominated by Sr derived from the original marine carbonates. Thus, the fluid is internally-
496 derived and released into the fracture from the adjacent protoliths. There is no need for an
497 externally-derived fluid prior infiltration of the mantle-like fluid. Guo et al. (2012, 2015)
498 show a comparable example, in which multistage epidote precipitation in a vein in UHP
499 eclogite first occurred from internally-derived fluids from the immediate eclogite, then from
500 externally-derived fluids during retrogression under amphibolite-facies conditions, by using
501 in-situ La-ICPMS Sr isotope data.
502 The fracture may have formed because of increased pore fluid pressure during subduction
503 (hydrofracture). Such an increase in pore fluid pressure may result from (i) a decrease of the
504 pore volume during subduction, (ii) dehydration reactions in the rocks, i.e. decomposition of
505 hydrous minerals (Getty and Selverstone, 1994; Zheng and Hermann, 2014), or (iii) the
506 infiltration of an external fluid into the rock. The titanite I acted as a sink for Sr released from
507 protolith limestone and for Al, Si, and Ti, possibly released from silicate minerals in the
508 marble, during prograde metamorphism.

509 The range of the $^{87}Sr/^{86}Sr$ ratios within the titanite core is small compared to the drastically
510 different Sr isotopic compositions between vein and matrix. The variation in Sr composition
511 in the titanite core demonstrates that there was no isotopic homogenization at the scale of the
512 megacryst. The variability reflects the availability of Sr from different sources (e.g., Romer
513 and Xiao, 2005; Romer and Rötzler, 2011). The range of Sr isotopic compositions in the core
514 may reflect contrasting contributions of Sr from carbonate and silicate minerals from the
515 marine limestone precursor during the growth of titanite.

516

517 ***5.1.2 Episode B, replacement of titanite I by rutile***

518 The large metastable titanite I crystal survived subduction to UHP conditions, deformation of
519 the marble, and exhumation and has only been incompletely replaced. Replacement of titanite
520 I is recorded by the presence of rutile, calcite, and quartz in the reaction rim according to the
521 reaction titanite + fluid (CO_2) ↔ rutile + quartz (coesite) + calcite (aragonite). This fluid-
522 mineral replacement occurred during episode B (Table 2; Fig. 6).

523 Based on the microfabric relationships of the shape-preferred orientation of rutile grains
524 parallel to the foliation of the marble matrix, we suggest that rutile in the rim of the titanite
525 megacryst formed during fluid-interaction and ductile deformation at the HP-UHP stage. In
526 calcsilicate marbles from the same unit, which have similar bulk rock compositions, but have
527 been less modified by retrogression, rutile belongs to the peak-PT mineral assemblage and
528 formed during prograde HP to UHP metamorphic conditions (Schmid et al., 2000).

529 The formation of rutile at the expense of titanite could result from the increase of CO_2 activity
530 in the fluid/rock system or/and the increase of pressure (Fig. 6). Low XCO_2 may favor the
531 stability of titanite even at ultrahigh pressures (Ye et al., 2002, Xiao et al. 2017). For instance,
532 banded UHP calcsilicate rocks with mineral assemblages containing either rutile or titanite
533 may result from centimeter-scale local heterogeneity in fluid compositions (XCO_2) during
534 UHP metamorphism/metasomatism (Ogasawara, 2014). Thus, the replacement of titanite I by
535 rutile and the back-reaction to titanite II and III could result from changes in the local
536 fluid/rock geochemical system or infiltration of an external fluid.

537 Microfabric observations, i.e. rutile alignment parallel to HP/UHP minerals, suggest that
538 changing XCO_2 due to fluid infiltration were not the sole cause for rutile formation during
539 episode B. Instead, rutile formed during prograde HP to UHP metamorphism associated with
540 deformation and pressure increase, in line with Schmid et al. (2001). The calculated rutile-in-
541 field for impure marbles agrees well with fluid-infiltration during subduction below 60 km
542 (~2 GPa).

543

544 ***5.1.3 Episode C, interaction with mantle-derived fluid and back-reaction to titanite***

545 Rutile is consumed by titanite II and titanite III, having higher and lower X_{Al}, respectively,
546 than titanite I (Fig. 2g; 2h). These small-scale variations of titanite chemistry reflect fluid-
547 interaction processes controlling the back-reaction to titanite II and III. The interfaces
548 between titanite I, II, III, and rutile are sharp. The irregular distribution of the chemically
549 different titanite II and III resembles the patchy titanite formed in the hydrothermal
550 experiments of Lucassen et al. (2010). These authors related the irregular Ti-Al zoning in
551 titanite replacing rutile to small-scale variations of fluid composition, reflecting one single
552 fluid-interaction process. In addition to the irregular patches, titanite II and III locally show
553 two chemically distinct, straight reaction fronts replacing titanite I (Supplement S3). In this
554 case replacement of high X_{Al} titanite II by low X_{Al} titanite III (Fig. 2d-f) may be related to
555 successive fluid-interaction episodes (C and D) during decompression (Carswell et al., 1996).

556 The re- or newly crystallized grains of titanite II and III grew at the expense of oriented rutile.
557 They show no indication for syn-deformative growth (Fig. 5a). Instead, the varying and large
558 degree of misorientation angles of the crystal lattice with respect to the titanite core and the
559 low-energy grain boundaries indicate progressive replacement under stress-free conditions.
560 This interpretation is supported by the increase of size of newly formed grains with increasing
561 distance from the rutile and is in accordance with matrix microfabrics that indicate
562 decomposition of HP-minerals under stress-free conditions during decompression. The
563 internal fabric of symplectites and replacement products of phengite suggest that the
564 subsequent episodes of fluid-rock interaction during decompression have not been
565 accompanied by ductile deformation of the matrix. This contrasts to the formation of rutile
566 during deformation, suggesting a change of the state of the imposed stress during the back-

567 reaction to titanite. This further supports the interpretation, that changing PT-conditions and
568 not solely changing XCO_2 controlled the back-reaction.

569 The minerals titanite (II/III), calcite, and albite in the reaction rim have lower $^{87}Sr/^{86}Sr$ values
570 than titanite I, recording infiltration and interaction with a fluid with mantle-like Sr, typical
571 for mantle-derived fluids. Sr isotope data from titanite I, together with all titanite and calcite
572 samples from the reaction rim (titanite II/III, calcite, Fig.4) fall on a two–component (end
573 member) mixing line. As a result of the dissolution-precipitation process, the Sr isotopic
574 composition of newly precipitated titanite (II and III) in the reaction rim between the titanite
575 megacryst and the marble matrix represents a mixture of Sr derived in different proportions
576 from the incoming fluid and the fluid from dissolved titanite I. Titanite I provides a local
577 source for Sr with high $^{87}Sr/^{86}Sr$ values, corresponding to the upper end-member (Fig. 4).

578 The $^{87}Sr/^{86}Sr$ values (c. 0.7053) of minerals within the reaction rim preserve an earlier state of
579 the infiltration history that is erased in the matrix. The original $^{87}Sr/^{86}Sr$ of the external fluid
580 might have been as low as 0.7037, indicated by the marble with the lowest $^{87}Sr/^{86}Sr$ (Fig. 1b;
581 Romer at al., 2003). During the course of migration through the marble, the external fluid
582 interacted with the marble minerals. Thus, the Sr isotopic composition of the fluid is shifted
583 towards more radiogenic values, whereas the Sr isotopic composition of the newly formed
584 minerals is shifted towards a less radiogenic Sr isotopic composition. Thus, the Sr isotopic
585 composition (c. 0.7053) of the reaction rim minerals does not reflect the original isotopic
586 composition of the external fluid that infiltrated the marble, but represents already a mixture.

587 The relict mineral assemblage (titanite II, III, and calcite) of the titanite reaction rim and its Sr
588 isotopic compositions (c. 0.7053) may document fluid-rock interaction (episode C) that is not
589 observed in the calcsilicate marble matrix (c. 0.7045), where it has been overprinted and
590 erased during the pervasive fluid-mineral-interaction episode D.

591

5.1.4 Episode D, pervasive interaction of the marble matrix with mantle-derived fluid

The reaction rim of the titanite megacryst records incomplete replacement. It is not clear whether replacement of high X_{Al} titanite II by low X_{Al} titanite III (Fig. 2d-f, Supplement S2) record two successive fluid-interaction episodes (C, D) during decompression. This may become only clear if these episodes are sufficiently separated in time to be resolved by U-Pb dating.

In contrast to the reaction rim, the marble matrix underwent pervasive recrystallization. The older mineral assemblage, including diopside, observed in impure marble from the Dabie UHP unit (Schmid et al., 2003; Liu et al., 2017), has been consumed in our sample under amphibolite facies conditions. Instead, the mineral phases calcite, titanite, amphibole, and clinozoisite formed during decompression from eclogite to amphibolite facies conditions (Fig. 6). The similar Sr isotopic composition of ~ 0.7045 (Table 1) of these minerals indicates that equilibration with the interacting fluid resulted in isotopic homogenization. The clinozoisite-titanite III pair from the matrix yields an $^{206}Pb/^{238}U$ age of 214±4 Ma for this reaction (Wawrzenitz et al., 2006). Elsewhere in Dabie Shan, this amphibolite facies retrogression has been dated at 218-214 Ma (e.g. Wu et al., 2006).

5.1.5 Episode E, late localized fluid infiltration

Allanite is rare and occurs in two different positions: (i) along calcite grain boundaries in the marble matrix and (ii) in fractures in the core of the large pre-UHP titanite (Fig. 2i-n). Allanite in both positions has a radiogenic $^{87}Sr/^{86}Sr$ value (0.7080), which is even higher than in the titanite core. This implies infiltration of a new fluid with a $^{87}Sr/^{86}Sr$ ratio of c. 0.7080, significantly more radiogenic than the previously infiltrated mantle-derived fluid (episode E).

615 In contrast to the mantle-derived fluid, this later fluid interacted only locally. This is
616 documented by the localized precipitation of (i) allanite at grain boundaries and along
617 fractures, (ii) dolomitic patches along the cleavage planes and Mg-rich carbonates around the
618 pores in calcite grains, and (iii) tiny sulfide minerals along these pore walls and in small
619 veins. This suggests that the previously formed porosity in the carbonate matrix served as
620 pathway of this late fluid. This fluid must have introduced LREE, Sr, Mg, and Th, now
621 incorporated in allanite, and Fe, Pb, and Sb, now precipitated as sulfides. Allanite replaced
622 titanite I by a coupled dissolution-precipitation mechanism. Since allanite has a much higher
623 Sr concentration than titanite, the additional Sr must have been introduced by the fluid and
624 was mainly incorporated into allanite.

625 Sr with more radiogenic composition, Th and LREE may derive from interaction of the fluid
626 with crustal rocks, e.g., para- and orthogneisses, that have been tectonically juxtaposed to the
627 marbles at episode E and that are intercalated with the marbles. These crustal rocks have
628 much higher initial $^{87}Sr/^{86}Sr$ values >0.7100 (Wawrzenitz et al., 2006).

629

630 **5.2 The role of deformation and fluid**

631 Combining the mineral-scale Rb-Sr isotope and microprobe data with microfabric and EBSD
632 studies allow for identifying mechanisms and pathways of fluid infiltration. During successive
633 episodes, the predominance of different processes related with Sr isotope exchange varied.

634

635 ***5.2.1 Titanite I crystallization in a hydrofracture***

636 During subduction, the breakdown of volatile-bearing mineral phases like dolomite, phengite,
637 clinozoisite, zoisite, and amphibole probably increased the fluid-pressure and induced

638 hydrofracturing. The vein hosting the titanite megacryst likely was such a hydrofracture that
639 formed during subduction. Far-field tectonic stress is not needed for this process.

640 During episode A, fluids were released from the adjacent wall rocks into hydrofractures. The
641 fractures may be sealed with the precipitating minerals. These vein-filling minerals and the
642 adjacent wall-rock minerals will be in equilibrium with the fluid. Partial replacement of this
643 assemblage (vein-filling/wall rock) may occur during a new interaction episode, when the
644 fluid is no longer in equilibrium with the original product assemblage (Bucher – Nurminen,
645 1989). Replacement products (in the vein and wall rock) will be in equilibration with the new
646 evolved fluid.

647

648 ***5.2.2 Stress-free growth of titanite in the reaction rim***

649 The replacement of titanite I by titanite II/III resulted in sharp boundaries between chemically
650 distinctive zones. This is diagnostic for dissolution-precipitation processes (Putnis, 2010;
651 Harlov et al., 2011). As the titanite I megacryst represents a porphyroclast within the foliation
652 of the marble, deformation is likely to have played an important role in creating of fluid
653 pathways. Crystal-plastic deformation may create low-angle subgrain boundaries and,
654 provides a mechanism that generates pathways for the fluid. EBSD mapping, however, does
655 not show low-angle grain boundaries or subgrain-rotation in the rim of the titanite megacryst
656 and there is no chemical change associated with the only subgrain mapped in the core of
657 titanite I (Fig. 5f). Thus, EBSD mapping implies that crystal-plastic deformation was not
658 active during the formation of the reaction rim and slip on dislocations did not significantly
659 influence the chemical and Sr isotopic composition of the titanite megacryst.
660 In contrast, the newly formed grains at the rim indicate recrystallization at low stress in
661 presence of a fluid. These grains show a high degree of misorientation with respect to each
662 other and to the orientation of the core of the titanite megacryst (Fig. 5a). Some titanite

663 portions in the rim show a lattice orientation identical to that of the core. These sections have
664 inherited their lattice orientation from titanite I (cf. Putnis 2010) and may have formed by a
665 coupled dissolution-precipitation process during episodes C and/or D.

666 The resorption fabrics of rutile replaced by titanite II/III (episodes C and D) show stress-free
667 growth. Furthermore, the increasing grain size of titanite II/III with increasing distance to
668 rutile demonstrates that this replacement process occurred under static conditions (Fig 5b).
669 This suggests that deformation ceased before episode C-D. The reaction of rutile to titanite
670 results in volume increase (Fig. 2g; h), which leads to fracturing of rutile. These fractures
671 propagate from etch pits at the rutile-titanite interface and were filled with titanite. Such
672 reaction-driven fracturing of rutile may accelerate the replacement process (Jamtveit et al.,
673 2009).

674

675 ***5.2.3 Pervasive versus localized fluid migration***

676 In agreement with the low stress conditions indicated by the microfabrics for titanite growth
677 in the reaction rim, the matrix minerals also recrystallized at low stress conditions. This
678 suggests that dissolution-precipitation reactions and not deformation-controlled mass
679 transport and isotope homogenization among calcite, titanite, clinozoisite, and amphibole in
680 the matrix (episodes C, D). The complete recrystallization of calcite records pervasive fluid
681 migration and interaction. Channelized fluid migration and mass transport in fluid films along
682 carbonate grain boundaries may not explain complete replacement and results in internal
683 zonation pattern of carbonate grains (Ferrando et al. 2017) and calcsilicate minerals (Liu et
684 al., 2017).

685 The porosity observed in the calcite grains is the result of the fluid-mediated replacement
686 (Harlov et al., 2005; Hövelmann et al., 2010), and provided fluid pathways to transport matter
687 from and to the reaction front (Putnis and Austrheim, 2010).

688 Fluid migration through the pores is highlighted by the dolomitic patches around the pores, as
689 well as the precipitation of tiny sulfide minerals within the pores. Fluid migration along grain
690 boundaries, cleavage planes and fractures, is indicated by precipitation of allanite in marble
691 matrix and titanite I. This demonstrates that porosity together with grain boundaries, cleavage
692 planes and fractures served as fluid channels during episode E, probably providing an
693 interconnected network. In contrast to earlier episodes, episode E did not result in complete
694 replacement of grains by dissolution-precipitation mechanisms.

695

696 ## Conclusion

697 The results are consistent with the following fluid-rock-interaction history:

698 • The prograde episode A is linked to subduction of the carbonate rock. Episode A is
699 related with interaction with an aqueous fluid sourced from dehydration reactions
700 in the impure marble or from subducting crustal rocks.

701 • Increasing overpressure during subduction results in hydrofracturing and the
702 formation of veins in which the titanite megacryst precipitated from fluids released
703 from the wall rocks of the impure marble (at ca. 244 Ma). This titanite acted as a
704 sink for HFSE and preserves the Sr isotopic composition of the late
705 Neoproterozoic marine carbonate protoliths ($^{87}Sr/^{86}Sr$ values of 0.7076-0.7072).

706 • Ongoing subduction and deformation with successive episodic fluid interaction
707 resulted in the growth of rutile at the titanite rim at HP-UHP conditions (episode

B). This episode is possibly, but not necessarily, related to infiltration of mantle-derived aqueous fluids with characteristic mantle-like Sr isotopic composition.

- During episode C, infiltration and interaction of mantle-derived fluid is indicated by the replacement of rutile by titanite II and possibly III, which formed in the reaction rim of the titanite megacryst and show reduced $^{87}Sr/^{86}Sr$ values (0.7055-0.7053). During successive dissolution-precipitation replacement, the precipitating titanite incorporated Sr derived from both the dissolved precursor mineral and the fluid.

- During episode D, the mantle-derived fluid mediated pervasive dissolution reprecipitation reactions in the marble matrix and probably in the reaction rim (titanite III). The mineral reaction history of the marble links episode D to post UHP — HP/amphibolite facies conditions at ca. 214 Ma (U-Pb isochron age, calculated with calcite and titanite from the matrix).

- Carbonate and silicate phases in the marble matrix show homogeneous, mantle-like $^{87}Sr/^{86}Sr$ (~0.7045), implying the matrix preserved only the signature of the final pervasive metasomatism. Successive pervasive dissolution-precipitation processes (episodes A-D) represent the mechanism that may metasomatize large volumes of carbonate rocks during subduction and exhumation.

- During episode E, channelized infiltration of fluids with a high $^{87}Sr/^{86}Sr$ value (>0.7080) occurred along grain boundaries, fractures, and pores. This late low-grade fluid triggered localized replacement reactions and precipitation of REE-rich allanite.

- The Sr isotopic compositions of the mineral phases that precipitated during the successive dissolution-precipitation processes reflect a mixing between the fluid from the dissolving precursor phases and the incoming fluids.
- Deformation was not a controlling factor during mineral replacement by dissolution-precipitation processes.

Our observations demonstrate multiphase metasomatism of impure marbles in the subduction zone by externally derived fluids. The mechanisms by which the infiltrating fluids interacted with the carbonates changed during the mineral-fluid-reaction history. Such multiphase fluid-rock interaction histories are revealed by (sub)mineral-scale isotope analyses, but not by conventional whole-rock analysis. Our results indicate that during deep subduction mantle-derived fluids may remove nearly completely the original crustal fingerprint of the marble.

Acknowledgements

This work was carried out as part of the research group FOR 741 'Nanoscale processes and geomaterials properties', sponsored by DFG code number DFG grant RO 2084/7-1. The titanite study has been motivated by a previous research project of N.W. with Roland Oberhänsli (Potsdam University) who kindly supplied the titanite sample.

The clarity of the paper was improved by the constructive reviews of Ralf Halama and an anonymous referee, and by the editorial comments of M. Scambelluri, which we highly appreciate.

We thank Dieter Rhede and Oona Appelt for help with the microprobe and Ilona Schäpan with the SEM (all at GFZ German Research Centre for Geosciences). We would like to thank our colleagues from DFG Forschergruppe FOR741, Friedrich Lucassen (Marum Bremen) and Gerlinde Habler (Vienna University) for cooperation and discussions. N.W. thanks Eric

Scherer (Münster University) and Gianluca Frijia (Potsdam University) for access to the New Wave Merchantek Drilling System, Jochen Rötzler (GFZ) for support with mineral chemical calculations, and Alexander Krohe (Münster University) for inspiring discussions and improving the readability of the text.

References

Ague, J. J., Nicolescu, S., 2014. Carbon dioxide released from subduction zones by fluid-mediated reactions. *Nature Geoscience*, *7*(5), 355-360.

Birck, J. L., 1986. Precision K- Rb- Sr isotopic analysis: application to Rb- Sr chronology. *Chemical geology*, *56*(1-2), 73-83.

Bucher-Nurminen, K., 1989. Reaction veins in marbles formed by a fracture-reaction-seal mechanism. European Journal of Mineralogy, 701-714.

Brower, F.M., Groen, M., Nebel, O., Wijbrans, J.R., Qiu, H.N., Yang, Q.J., Zhao, L.H., Wu, Y.B., 2011. Coherence of the Dabie Shan UHPM terrane investigated by Lu-Hf and 40r/39Ar dating of eclogites. In L. Dobrzhinetskaya, S. Cuthbert, W. Faryad, S. Wallis (Eds.), UHPM: 25 years after discovery of coesite and diamond (pp. 325-357). https:doi.org/10.1016/B978-0-12-385144-4.00010-2

Bryant, D. L., Ayers, J. C., Gao, S., Miller, C. F., Zhang, H., 2004. Geochemical, age, and isotopic constraints on the location of the Sino–Korean/Yangtze Suture and evolution of the Northern Dabie Complex, east central China. Geological Society of America Bulletin, 116, 5-6), 698-717.

777 Carswell, D. A., Wilson, R.N., Zhai, M., 1996. Ultra-high pressure aluminous titanites in
778 carbonate-bearing eclogites at Shuanghe in Dabieshan, central China. Mineralogical
779 Magazine, 60, 400, 461-471. https://doi.org/10.1180/minmag.1996.060.400.07

780 Charlier, B.L.A., Ginibre, C., Morgan, D., Nowell, G.M., Pearson, D.G., Davidson, J.P.,
781 Ottley, C.J., 2006. Methods for the microsampling and high-precision analysis of strontium
782 and rubidium isotopes at single crystal scale for petrological and geochronological
783 applications. Chem. Geol. 232, 114–133.

784 Fein, J.B., Graham, C.M., Holness, M.B., Fallick, A.E., Skelton, A.D.L., 1994. Controls on
785 the mechanisms of fluid infiltration and front advection during regional metamorphism: a
786 stable isotope and textural study of retrograde Dalradian rocks of the SW Scottish Highlands.
787 J. Metam. Geol., 12, 249-260.

788 Faure, M., Lin, W., Schärer, U., Shu, L., Sun, Y., Arnaud, N., 2003. Continental subduction
789 and exhumation of UHP rocks. Structural and geochronological insights from the Dabieshan
790 (East China). *Lithos*, *70*(3-4), 213-241.

791 Ferrando, S., Groppo, C., Frezzotti, M. L., Castelli, D., Proyer, A., 2017. Dissolving dolomite
792 in a stable UHP mineral assemblage: Evidence from Cal-Dol marbles of the Dora-Maira
793 Massif (Italian Western Alps). *American Mineralogist*, *102*(1), 42-60.

794 Franz, L., Romer, R. L., Klemd, R., Schmid, R., Oberhansli, R., Wagner, T., Shuwen, D.
795 2001, Eclogite-facies quartz veins within metabasites of the Dabie Shan (eastern China):
796 Pressure-temperature-time-deformation-path, composition of the fluid phase and fluid flow
797 during exhumation of high-pressure rocks. Contrib. Mineral. Petrol., 141, 322–346.

798 Frezzotti, M. L., Selverstone, J., Sharp, Z. D., Compagnoni, R., 2011. Carbonate dissolution
799 during subduction revealed by diamond-bearing rocks from the Alps. *Nature Geoscience*,
800 *4*(10), 703.

801 Getty, S. R., Selverstone, J., 1994. Stable isotopic and trace element evidence for restricted
802 fluid migration in 2 GPa eclogites. *Journal of metamorphic Geology*, *12*(6), 747-760.

803 Guo, S., Ye, K., Chen, Y., Liu, J., Mao, Q., Ma, Y.G., 2012. Fluid-rock interaction and
804 element mobilization in UHP metabasalt: Constraints from an omphacite epidote vein and
805 host eclogites in the Dabie orogeny. Lithos 136-139, 145-167.

806 Guo, S., Chen, Y., Ye, K., Su, B., Yang, Y.H., Zhang, L.M., Liu, J.B., Mao, Q., 2015.
807 Formation of multiple high-pressure veins in ultrahigh-pressure eclogite (Hualiangting, Dabie
808 terrane, China): Fluid source, element transfer, and closed-system metamorphic veining.
809 *Chemical Geology*, *417*, 238-260.

810 Hacker, B.R., Ratschbacher, L., Liou, J.G., 2004. Subduction, collision, and exhumation in
811 the ultrahigh-pressure Qinling-Dabie orogen. Geological Society, London, Special
812 Publications 226, 1, 157-175.

813 Hacker, B. R., Wallis, S. R., Ratschbacher, L., Grove, M., Gehrels, G., 2006. High□
814 temperature geochronology constraints on the tectonic history and architecture of the
815 ultrahigh□pressure Dabie□Sulu Orogen. *Tectonics*, *25*(5).

816 Harlov, D. Wirth, R., Förster, H.-J., 2005. An experimental study of dissolution-precipitation
817 in fluorapatite: Fluid infiltration and the formation of monazite. Contributions to Mineralogy
818 and Petrology, 150, 3, 268-286. http://doi.org/10.1007/s00410-005-0017-8.

819 Harlov, D., Wirth, R., Hetherington, C.J. 2011. Fluid-mediated partial alteration in monazite:
820 the role of coupled dissolution–reprecipitation in element redistribution and mass transfer.
821 Contrib. Mineral. Petrol. 162, 329–348.

822 Herman, J., Spandler, C., Hack, A., Korsakov, A.V., 2006. Aqueous fluids and hydrous melts
823 in high-pressure and ultra-high pressure rocks: implications for element transfer in subduction
824 zones. Lithos, 92, 399–417.

825 Hielscher, R., Schaeben, H. 2008. A novel pole figure inversion method: specification of the
826 MTEX algorithm. Journal of Applied Crystallography 41, 1024-1037.

827 Hövelmann, J., Putnis, A., Geisler, T., Schmidt, B.C., Golla-Schindler, U., 2010. The
828 replacement of plagioclase feldspars by albite: observations from hydrothermal experiments.
829 Contributions to Mineralogy and Petrology, 159, 1, 43-59. http://doi.org/10.1007/s00410-009-
830 0415-4.

831 Holness, M.B., Graham, C.M., 1995. P-T-X effects on equilibrium carbonate-H2O-CO2-NaCl
832 dihedral angles: constraints on carbonate permeability and the role of deformation during
833 fluid infiltration. Contributions to Mineralogy and Petrology, 119, 2-3, 301-313.
834 http://doi.org/10.1007/s004100050044

835 Jacobsen, S.B., Kaufman, A.J., 1999. The Sr, C and O isotopic evolution of Neoproterozoic
836 seawater. Chemical Geology 161, 37-57.

837 Jamtveit, B. Putnis, C.V., Malthe-Sorensen, A., 2009. Reaction induced fracturing during
838 replacement processes. Contributions to Mineralogy and Petrology, 157, 1, 127-133.

839 Li, X. P., Zheng, Y. F., Wu, Y. B., Chen, F., Gong, B., Li, Y. L., 2004. Low-T eclogite in the
840 Dabie terrane of China: petrological and isotopic constraints on fluid activity and radiometric
841 dating. *Contributions to Mineralogy and Petrology*, *148*(4), 443-470.

842 Li, S., Kusky, T. M., Zhao, G., Liu, X., Wang, L., Kopp, H., Hoernle, K., Zhang, G., Dai, L.
843 2012. Thermochronological constraints on two-stage extrusion of HP/UHP terranes in the
844 Dabie–Sulu orogen, east-central China. *Tectonophysics*, *504*(1-4), 25-42.

845 Liu, P., Wu, Y., Chen, Y., Zhang, J., Jin, Z. (2015). UHP impure marbles from the Dabie
846 Mountains: Metamorphic evolution and carbon cycling in continental subduction zones.
847 *Lithos*, *212*, 280-297.

Liu, F.L., Gerdes, A., Liou, J.G., Xue, H.M., Liang, F.H. (2006). Shrimp U-Pb zircon dating from Sulu-Dabie dolomitic marble, eastern China: constraints on prograde, ultrahigh-pressure and retrograde metamorphic ages. *Journal of Metamorphic Geology*, 24, 7, 569-589. https://doi.org/10.1111/j.1525-1314.2006.00655.x

Liu, P., Massonne, H.-J., Jin, Z., Wu, Y., Zhang, J. (2017). Diopside, apatite, and rutile in an ultrahigh pressure impure marble from the Dabie Shan, eastern China: A record of eclogite-facies metasomatism during exhumation. *Chemical Geology*, 466, 123-139. DOI 10.1016/j.chemgeo.2017.06.001

Lucassen, F., Franz, G., Rhede, D., Wirth, R., 2010. Ti-Al zoning of experimentally grown titanite in the system CaO-Al2O3-TiO2-SiO2-NaCl-H2O-(F): Evidence for small-scale fluid heterogeneity. *American Mineralogist*, Volume 95, 1365–1378, 2010.

Lucassen, F., Franz, G., Dulski, P., Romer, R. L., Rhede, D., 2011. Element and Sr isotope signatures of titanite as indicator of variable fluid composition in hydrated eclogite. *Lithos*, *121*(1-4), 12-24.

Ma, C., Ehlers, C., Xu, C., Li, Z., & Yang, K. (2000). The roots of the Dabieshan ultrahigh-pressure metamorphic terrane: constraints from geochemistry and Nd–Sr isotope systematics. *Precambrian Research*, *102*(3-4), 279-301.

Manning, C. E. (2014). Geochemistry: A piece of the deep carbon puzzle. *Nature Geoscience*, *7*(5), 333-334.

McArthur, J. M., Donovan, D. T., Thirlwall, M. F., Fouke, B. W., & Mattey, D. (2000). Strontium isotope profile of the early Toarcian (Jurassic) oceanic anoxic event, the duration of ammonite biozones, and belemnite palaeotemperatures. *Earth and Planetary Science Letters*, 179(2), 269-285.

871 Ogasawara, Y. 2014. Titanite stability in UHP metacarbonate rocks from the Kokchetav
872 Massif, Northern Kazakhstan. *Gakujutsu Kenkyu (Academic Studies and Scientific Research)*
873 *Natural Science*, *62*, 11-31.

874 Ohta, M., Mock, T., Ogasawara, Y., Rumble, D., 2003. Oxygen, carbon, and strontium
875 isotope geochemistry of diamond-bearing carbonate rocks from Kumdy-Kol, Kokchetav
876 Massif, Kazakhstan. *Lithos*, *70*(3-4), 77-90.

877 Okay, A.I., Xu, S.T. Sengor, A.M.C., 1989. Coesite from the Dabie Shan eclogites, central
878 China: European Journal of Mineralogy, 1, 4, 595-598.

879 Oliver, N. H., Bons, P. D., 2001. Mechanisms of fluid flow and fluid–rock interaction in fossil
880 metamorphic hydrothermal systems inferred from vein–wallrock patterns, geometry and
881 microstructure. *Geofluids*, *1*(2), 137-162.

882 Pin, C., Bassin, C., 1992. Evaluation of a strontium-specific extraction chromatographic
883 method for isotopic analysis in geological materials. *Analytica Chimica Acta*, *269*(2), 249-
884 255.

885 Prave, A. R., Meng, F. W., Lepland, A., Kirsimäe, K., Kreitsmann, T., Jiang, C. Z., 2018. A
886 refined late-Cryogenian–Ediacaran earth history of South China: Phosphorous-rich marbles of
887 the Dabie and Sulu orogens. *Precambrian Research*, *305*, 166-176.

888 Prior, D.J., Boyle, A.P., Brenker, F., Cheadle, M.C., Day, A., Lopez, G., Peruzzo, L., Potts,
889 G.J., Reddy, S.M., Spiess, R., Trimby, P.W., Wheeler, J., Zetterstroöm, L., 1999. The
890 application of electron back-scatter diffraction and orientation contrast imaging in the SEM to
891 textural problems in rocks. American Mineralogist 84, 1741-1759.

892 Prokoph, A., Shields, G. A., & Veizer, J., 2008. Compilation and time-series analysis of a
893 marine carbonate δ18O, δ13C, 87Sr/86Sr and δ34S database through Earth history. *Earth-*
894 *Science Reviews*, *87*(3-4), 113-133.

895 Putnis, A., 2009. Mineral replacement reactions. Reviews in Mineralogy and Geochemistry,
896 70, 1, 87-124. Doi 10.2138/rmg.2009.70.3

897 Putnis, A., Austrheim, H., 2010. Fluid-induced processes: metasomatism and metamorphism.
898 Geofluids, 10, 254–269.

899 Romer, R. L., 2001. Lead incorporation during crystal growth and the misinterpretation of
900 geochronological data from low□$^{238}U/^{204}Pb$ metamorphic minerals. *Terra Nova*, *13*(4), 258-
901 263.

902 Romer, R. L., Wawrzenitz, N., Oberhänsli, R., 2003. Anomalous unradiogenic $^{87}Sr/^{86}Sr$ ratios
903 in ultrahigh-pressure crustal carbonates–evidence for fluid infiltration during deep
904 subduction? *Terra Nova*, *15*(5), 330-336.

905 Romer, R.L., Xiao, Y., 2005. Initial Pb–Sr(–Nd) isotopic heterogeneity in a single allanite–
906 epidote crystal: implications of reaction history for the dating of minerals with low parent-to-
907 daughter ratios. Contrib Mineral Petrol 148, 662-674.

908 Romer, R.L., Rötzler, J., 2011. The role of element distribution for the isotopic dating of
909 metamorphic minerals. European Journal of Mineralogy, 23(1), 17-33. European Journal of
910 Mineralogy 23(1):17-33. DOI: 10.1127/0935-1221/2011/0023-2081

911 Rumble III, D., Wang, Q., Zhang, R., 2000. Stable isotope geochemistry of marbles from the
912 coesite UHP terrains of Dabieshan and Sulu, China. *Lithos*, *52*(1-4), 79-95.

913 Rumble III, D., Liou, J.G., Jahn, B.-M., 2003. Continental crust subduction and ultrahigh
914 pressure metamorphism. Treatise Geochem. 3, 293–319.

915 Schmid, R., Franz, L., Oberhänsli, R., Dong, S., 2000. High-Si phengite, mineral chemistry
916 and P–T evolution of ultra□high□pressure eclogites and calc-silicates from the Dabie Shan,
917 eastern China. *Geological Journal*, *35*(3□4), 185-207.

Schmid, R., 2001. Geology of ultra-high-pressure rocks from the Dabie Shan, eastern China. Diss. Inst. Geowiss. Universität Potsdam, p. 141.

Schmidt, M. W., & Poli, S. (2014). 4.19 Devolatilization During Subduction. In *Treatise on Geochemistry (Second Edition)* (pp. 669-701).

Sheng, Y. M., Zheng, Y. F., Li, S. N., Hu, Z., 2013. Element mobility during continental collision: insights from polymineralic metamorphic vein within UHP eclogite in the Dabie orogen. *Journal of Metamorphic Geology*, *31*(2), 221-241.

Spandler, C., Hammerli, J., Sha, P., Hilbert-Wolf, H., Hu, Y., Roberts, E., Schmitz, M., 2016. MKED1: A new titanite standard for in situ analysis of Sm-Nd isotopes and U-Pb geochronology. *Chemical Geology, 425*, 110-126.

Tao, R., Zhang, L., Li, S., Zhu, J., Ke, S., 2018. Significant contrast in the Mg-C-O isotopes of carbonate between carbonated eclogite and marble from the S.W. Tianshan UHP subduction zone: Evidence for two sources of recycled carbon. *Chemical Geology, 483*, 65–77.

Villa, I. M., De Bièvre, P., Holden, N. E., Renne, P. R., 2015. IUPAC-IUGS recommendation on the half life of 87Rb. *Geochimica et Cosmochimica Acta*, *164*, 382-385.

Veizer, J., Ala, D., Azmy, K., Bruckschen, P., Buhl, D., Bruhn, F., Carden, G.A.F., Diener, A., Ebneth, S., Godderis, Y., Jasper, T., Korte, C., Pawellek, F., Podlaha, O.G. and Strauss, H., 1999. $^{87}Sr/^{86}Sr$, $d^{13}C$ and $d^{18}O$ evolution of Phanerozoic seawater. Chem. Geol., 161, 59–88.

Wang, X.M., Liou, J.G., 1993. Ultra-high-pressure metamorphism of carbonate rocks in the Dabie Mountains, central China. Journal of Metamorphic Geology, 11, 4, pp. 575-588. DOI: 10.1111/j.1525-1314.1993.tb00173.x

941 Wang, X., Neubauer, F., Genser, J., Yang, W., 1998. The Dabie UHP unit, central China: A
942 Cretaceous extensional allochthon superposed on a Triassic orogen. *Terra Nova-Oxford*,
943 *10*(5), 260-267.

944 Wang, Q., Rumble, D., 1999. Oxygen and carbon isotope composition from the UHP
945 Shuanghe marbles, Dabie Mountains, China. Sci. China Ser. D-Earth Sci. 42: 88.
946 DOI:10.1007/BF02878502

947 Wang, S. J., Li, S. G., An, S. C., Hou, Z. H., 2012. A granulite record of multistage
948 metamorphism and REE behavior in the Dabie orogen: constraints from zircon and rock-
949 forming minerals. *Lithos*, *136*, 109-125.

950 Wang, S.-J., Teng, F.-Z., Li, S.-G., 2014. Tracing carbonate–silicate interaction during
951 subduction using magnesium and oxygen isotopes. Nat. Commun. 5:5328, DOI:
952 10.1038/ncomms6328

953 Wawrzenitz, N., Romer, R. L. Oberhänsli, R., Dong, S., 2006. Dating of subduction and
954 differential exhumation of UHP rocks from the Central Dabie Complex (E-China):
955 Constraints from microfabrics, Rb–Sr and U–Pb isotope systems, *Lithos*, **89**, 1-2, 174.

956 Wawrzenitz, N., Krohe, A., Rhede, D., Romer, R.L., 2012. Dating rock deformation with
957 monazite: The impact of dissolution-precipitation creep. Lithos, 134, 135, 52-74. DOI:
958 10.1016/j.lithos.2011.11.025

959 Wawrzenitz, N., Krohe, A., Baziotis, I., Mposkos, E., Kylander-Clark, A. R., & Romer, R. L.,
960 2015. LASS U–Th–Pb monazite and rutile geochronology of felsic high-pressure granulites
961 (Rhodope, N Greece): Effects of fluid, deformation and metamorphic reactions in local
962 subsystems. Lithos, 232, 266-285.

963 White, W. M., 2010. Oceanic island basalts and mantle plumes: the geochemical perspective.
964 *Annual Review of Earth and Planetary Sciences*, *38*, 133-160.

965 Whitney, D. L., Bernard W. E., 2010. Abbreviations for names of rock-forming minerals.
966 American mineralogist 95.1, 185.

967 Wu, Y.-B., Zheng, Y.-F., Zhao, Z.-F., Gong, B., Liu X., Wu F.-Y., 2006. U–Pb, Hf and O
968 isotope evidence for two episodes of fluid-assisted zircon growth in marble-hosted eclogites
969 from the Dabie orogen. Geochimica et Cosmochimica Acta 70, 3743–3761.

970 Wu, Y. B., Zheng, Y. F., 2013. Tectonic evolution of a composite collision orogen: an
971 overview on the Qinling–Tongbai–Hong'an–Dabie–Sulu orogenic belt in central China.
972 *Gondwana Research*, *23*(4), 1402-1428.

973 Xu, S., Liu, Y., Chen, G., Compagnoni, R., Rolfo, F., He, M., Liu, H. 2003. New findings of
974 Micro-diamonds in eclogites from Dabie-Sulu region in central-eastern China. Chin. Sci.
975 Bull., 2003, 48, 988. Doi 10.1007.BF03184213

976 Ye, K., Liu, J., Cong, B., Ye, D., Xu, P., Omori, S., Maruyama, S., 2002. Ultrahigh-pressure
977 (UHP) low-Al titanites from carbonate-bearing rocks in Dabieshan-Sulu UHP terrane, eastern
978 China. American Mineralogist, v. 87, 875-881.

979 Zhang, Z. M., Shen, K., Liou, J. G., Dong, X., Wang, W., Yu, F., & Liu, F., 2011. Fluid–rock
980 interactions during UHP metamorphism: A review of the Dabie–Sulu orogen, east-central
981 China. *Journal of Asian Earth Sciences*, *42*(3), 316-329.

982 Zheng, Y. F., Zhou, J. B., Wu, Y. B., Xie, Z., 2005. Low-grade metamorphic rocks in the
983 Dabie-Sulu orogenic belt: A passive-margin accretionary wedge deformed during continent
984 subduction. *International Geology Review*, *47*(8), 851-871.

985 Zheng, Y.-F., Gao, T.-S., Wu Y.-B., Gong, B., 2007. Fluid flow during exhumation of deeply
986 subducted continental crust: zircon U-Pb age and O-isotope studies of a quartz vein within
987 ultrahigh-pressure eclogite. Journal of Metamorphic 25, 267–28.

988 Zheng, Y.F., 2009. Fluid regime in continental subduction zones: petrological insights from
989 ultrahigh-pressure metamorphic rocks. Journal of the Geological Society, 166, 4, 763–782.
990 Zheng, Y.-F., Xia, Q.-X., Chen, R.-X., Gao, X.-Y., 2011. Partial melting, fluid supercriticality
991 and element mobility in ultrahigh-pressure metamorphic rocks during continental collision.
992 Earth-Science Reviews, 107, 342–374.

Figure captions

Fig. 1. The studied rock sample is a calcsilicate marble from the Changpu area, UHP unit in the Dabie Shan. a) Location map with $^{87}Sr/^{86}Sr$ ratios of marbles from the Changpu Unit. The studied sample is marked by an asterisk. Modified after Schmid, 2001; Romer et al., 2003 and Zheng et al., 2005.

b) Diagram showing Sr content in ppm vs. $^{87}Sr/^{86}Sr$ ratios from calcium carbonate data from the metasomatized marbles. Calcite with highest Sr contents show mantle-like $^{87}Sr/^{86}Sr$ ratios. Calcite data from the studied sample (rhombs) plots on the mixing line defined by the samples with the highest and lowest Sr isotope values, respectively.

c) The marble sample selected for this study. The marble matrix hosts a titanite megacryst. The foliation is recorded by the elongated shape of minerals and deflects around the megacryst.

Fig. 2. BSE images and element distribution maps of the sample. Mineral abbreviations as in Whitney and Bernhard (2010). For details see text. Fig. 2a shows the microsampling sites. 2b) Elongated shape of symplectites defining foliation. 2c) Titanite at the rim of phengite recording retrograde mineral reaction and decomposition of older high-Ti phengite. 2d) Element distribution map showing the homogeneous titanite core (titanite I) and the patchy rim with titanite II (high Al content) and III (low Al content). 2e and f) Element distribution maps (Ti and Al content, respectively) showing the irregular distribution of titanite II and III. 2g and h) BSE and Ti distribution map showing the replacement of rutile by titanite II. Cleavage planes in titanite I acted as fluid pathways. The reaction results in volume increase, visible at the domed reaction interface, and fracturing of rutile with fractures propagating from etch pits. Resorption microstructures record displacement of the former rutile phase boundary. 2i and j) BSE and Al distribution map showing the replacement of allanite at the

1018 expense of titanite I. Allanite precipitated along a fracture. 2k) BSE map showing the
1019 replacement of titanite by allanite. 2l and m) Replacement is related to fracturing of titanite I
1020 and to patchy allanite with variations of Ca and REE contents. 2n) Ti enrichment in titanite I
1021 adjacent to allanite related to reincorporation of Ti in titanite I during the dissolution-
1022 precipitation reaction.

1023

1024 Fig. 3a. BSE image of calcite showing reaction-induced porosity and precipitation of sulfides
1025 (pyrite) in pore walls. 3b) Ca-Mg-(Fe+Mn) diagram shows the chemical composition of
1026 carbonates in distinct microstructural positions.

1027

1028 Fig. 4. ^{87}Sr /^{86}Sr isotopic ratios (calculated for 240 Ma) vs. Sr concentration. Two samples,
1029 the one with the lowest (titanite I sample) and the one with the highest Sr concentration
1030 (titanite rim sample), have been used for calculation. All other samples from the reaction rim
1031 plot along this two-component mixing curve. Their respective position on the mixing
1032 hyperbola reflects the mixing of Sr from both sources (titanite I and fluid, in different
1033 proportions) in the minerals precipitating in the reaction rim. Titanite I provides a local source
1034 for Sr with higher $^{87}Sr/^{86}Sr$ values, corresponding to the crustal end-member (original impure
1035 carbonates). The interacting fluid corresponds to the mantle-like end-member. The isotopic
1036 composition of the incoming fluid may have shifted towards higher $^{87}Sr/^{86}Sr$ values before it
1037 reached the titanite rim due to interaction and mixing processes with the matrix minerals. The
1038 $^{87}Sr/^{86}Sr$ value of the fluid source, however, may be ≤ 0.7037, as reflected by the purest
1039 marbles in the Changpu unit.

1040 The Al-F - rich and Al-F - poor domains of the titanite rim could not be sampled separately.
1041 Therefore, the Sr isotopic composition of the Al-F poor domains (titanite III) is not known.
1042 The Sr isotopic composition of titanite III in the rim and pure calcite from the reaction rim

1043 constrains the less radiogenic end of the mixing line of ca. 0.7053, which differs from the
1044 composition of matrix calcite (0.7045). The Sr isotopic composition of titanite III reflects
1045 variable re-incorporation of Sr from titanite I during dissolution-precipitation reactions rather
1046 than mechanical mixing of *two* isotopically distinct titanite types. Note, titanite in the matrix
1047 showing the same chemical compositions as titanite III, has a $^{87}Sr/^{86}Sr$ value of 0.7045 (Table
1048 1), which corresponds to the composition of matrix calcite.

1049

1050 Fig. 5. Inverse pole figure (IPF) orientation maps (a, c, e) and phase maps (b, d, f) generated
1051 via Electron Backscatter Diffraction (EBSD). The maps illustrate the grain microstructures in
1052 titanite core and rim, and rutile, calcite and quartz in the reaction rim. Grain boundaries in the
1053 phase maps (b, d, f) are boundaries with misorientation angles >10°.

1054 Color scheme for grain orientation of titanite (in a) is given in the hemicircle. The titanite core
1055 lacks internal deformation and subgrain rotation (homogeneous pale green). The titanite rim
1056 consists of individual grains showing varying degrees of misorientation with respect to the
1057 core.

1058 Maps c and d show titanite, rutile and calcite, that all lack internal deformation and subgrain
1059 boundaries. Maps e and f show the homogeneous titanite core with local subgrain formation
1060 along a fracture. Note the small angle (≤ 3°) of misorientation.

1061

1062 Fig. 6. Schematic PT-loop (modified after Romer et al., 2003; Schmid, 2001; Carswell et al.,
1063 2000) showing the likely conditions of successive episodes of fluid-rock interaction during
1064 subduction to mantle depth and subsequent exhumation. The position of the titanite vs. rutile
1065 forming reaction depends on XCO_2 (dashed lines). Higher XCO_2 shifts the curve to higher

1066 temperatures. For details on the calculation of the reaction curves see Romer et al. (2003), p.

1067 334. Mineral abbreviations as in Whitney and Bernhard (2010).

1068

Wawrzenitz et al. Fig. 1

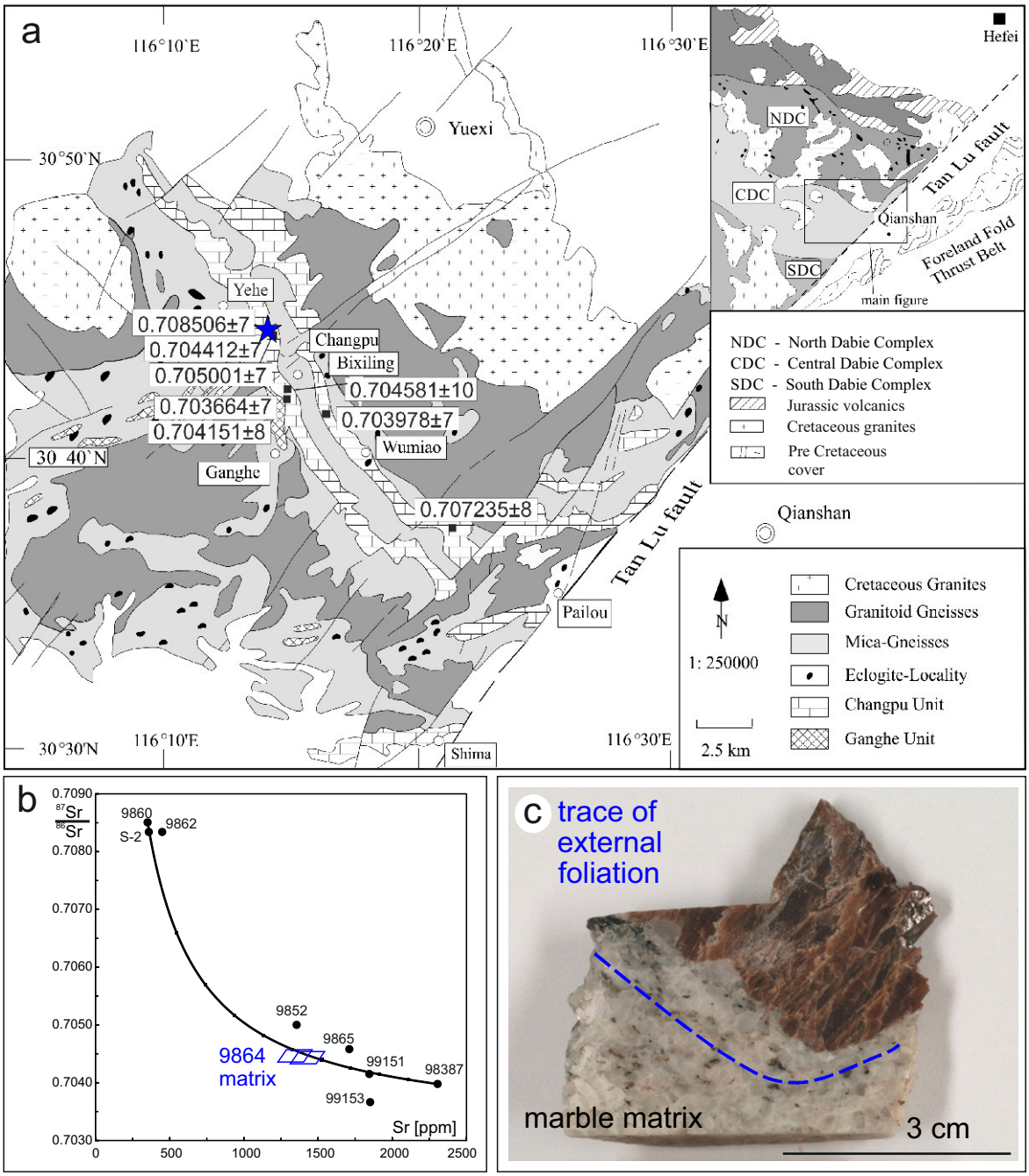

Wawrzenitz et al. Fig. 2

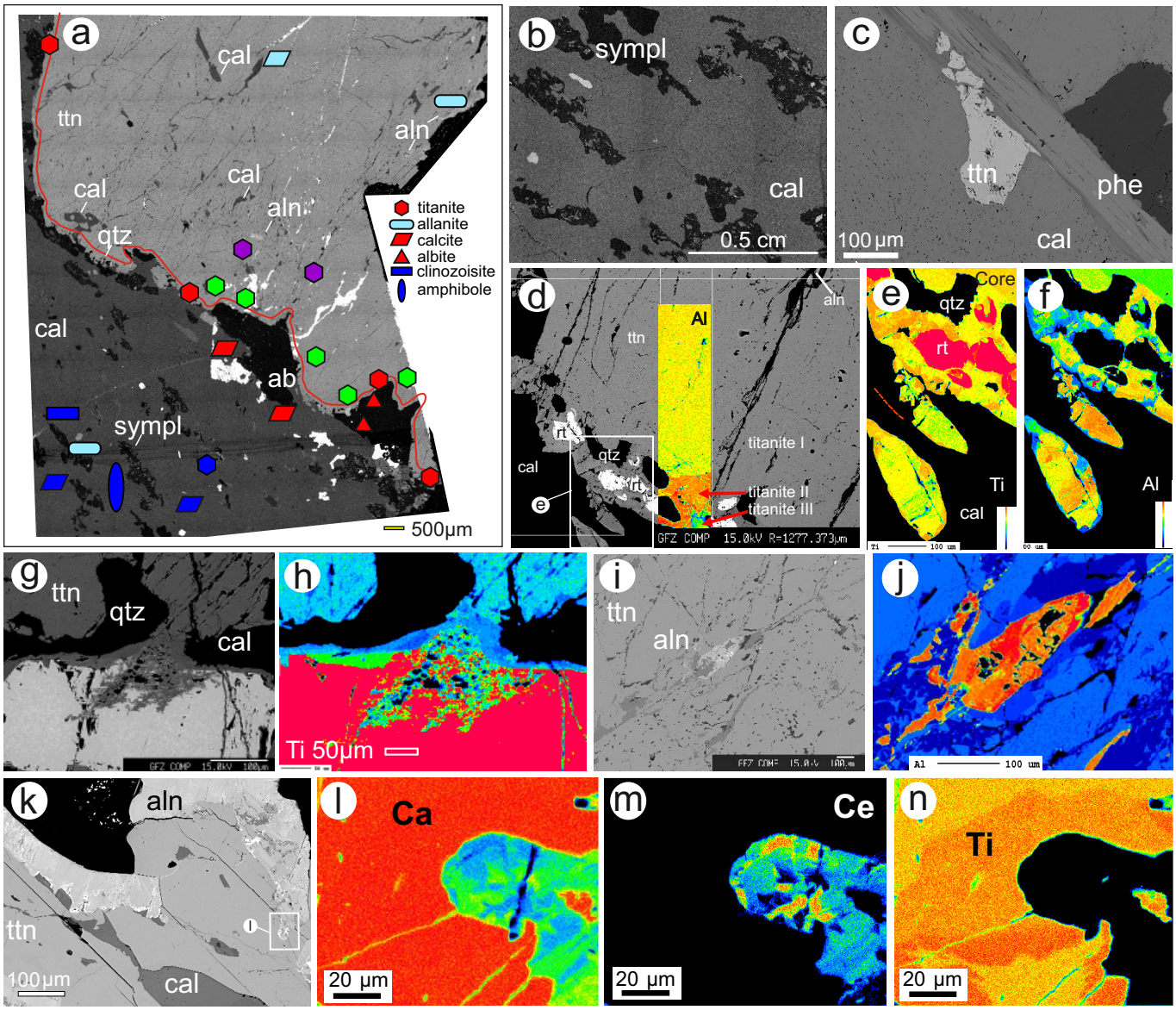

Wawrzenitz et al. Fig. 3

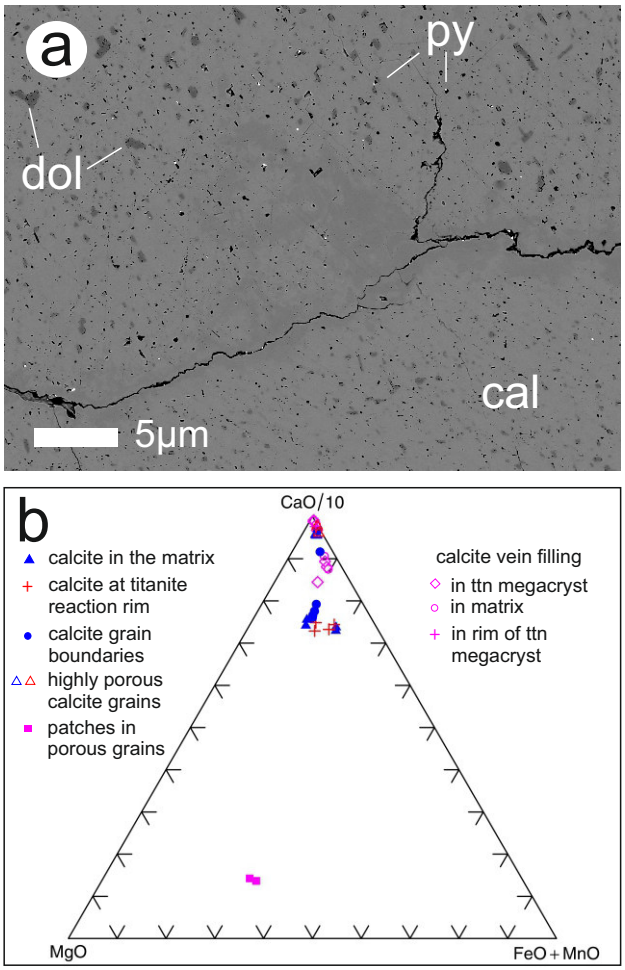

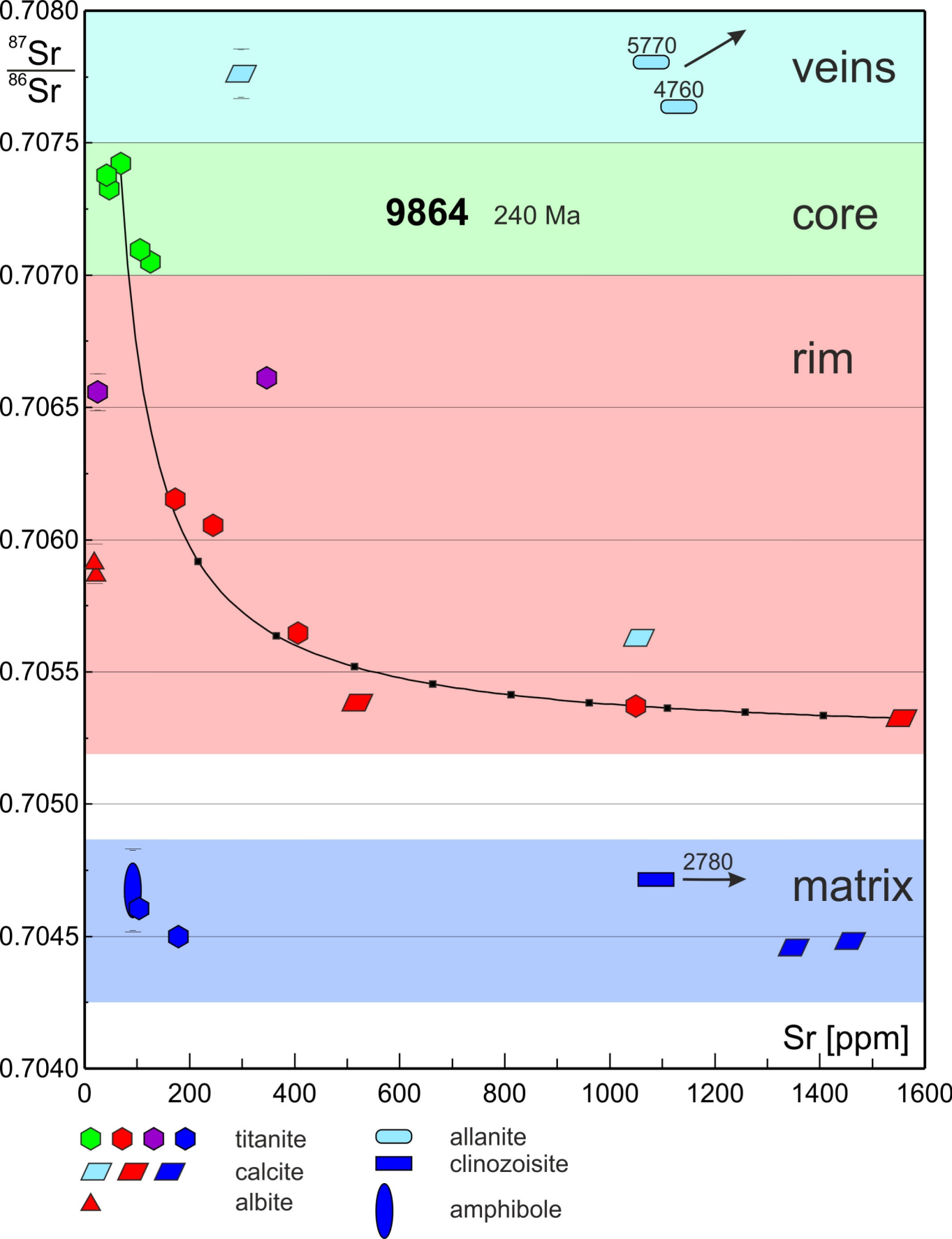
$^{87}Sr/^{86}Sr$
0.7080
0.7075
0.7070
0.7065
0.7060
0.7055
0.7050
0.7045
0.7040
0
200
400
600
800
1000
1200
1400
1600
Sr [ppm]
veins
core
rim
matrix
9864
240 Ma
5770
4760
2780
titanite
calcite
albite
allanite
clinozoisite
amphibole

Wawrzenitz et al. Fig. 5

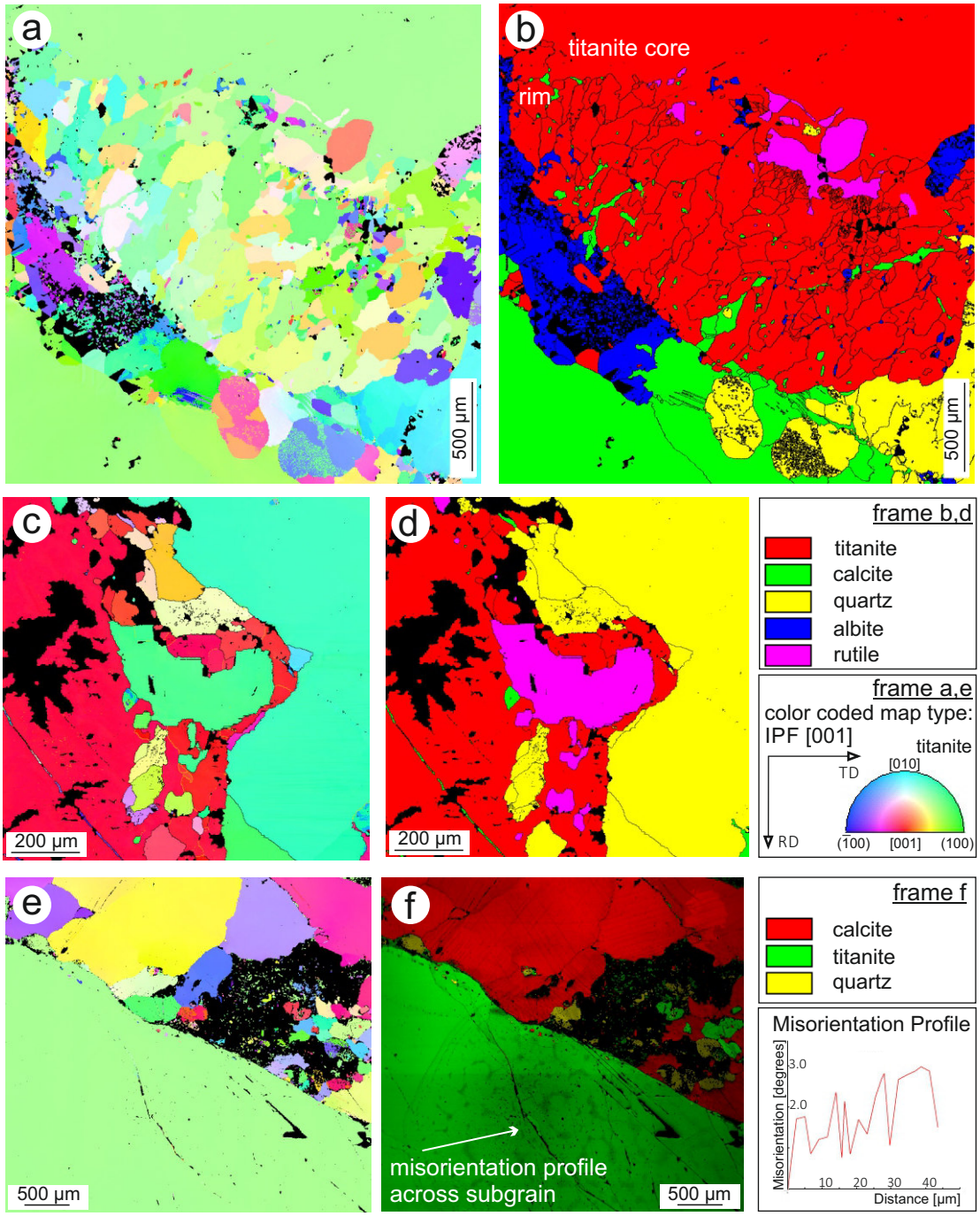

Fig. 6 Wawrzenitz et al.

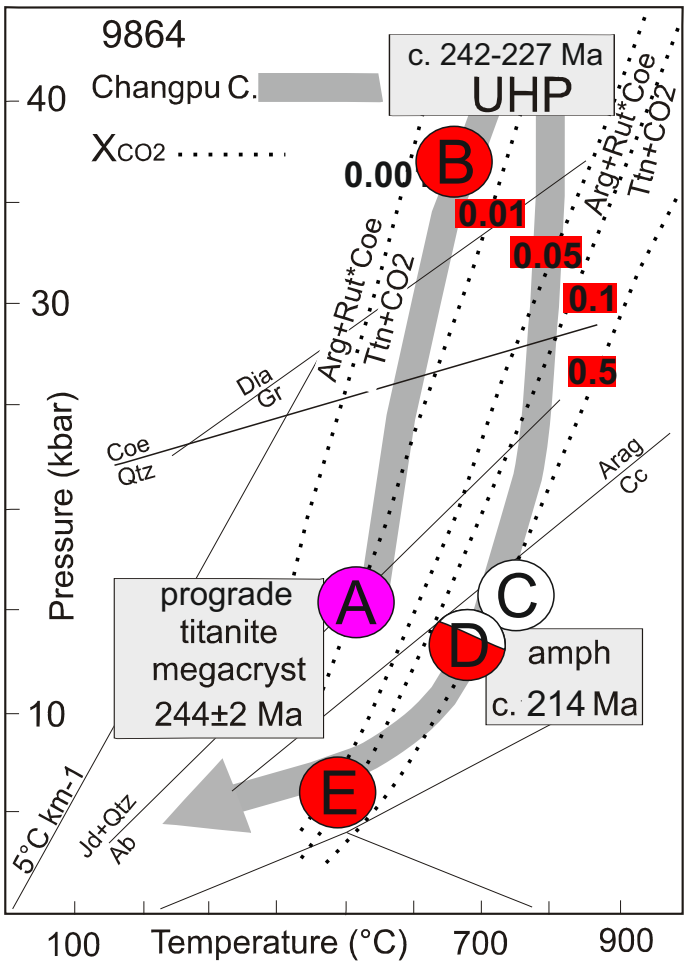

Table 1. Rb-Sr isotope data for titanite megacryst and minerals from its matrix.

Sample phase		Sample no.	Sample	Rb [ppm][a]	Sr [ppm][a]	$^{87}Rb/^{86}Sr$	$^{87}Sr/^{86}Sr$	$\pm 2\sigma_m$	$^{87}Sr/^{86}Sr_{240}$[c]	$^{87}Sr/^{86}Sr_{214}$[c]	$\pm 2\sigma_m$
			Core								
9864cb1-ttn-trench1	1 core	NH-11-5	Titanite	0.56	67.8	0.0241	0.70752	0.00001	0.70744	0.70745	0.00001
9864cb1-ttn-trench3	4 core	NH-11-24	Titanite	0.64	43.8	0.0423	0.70751	0.00003	0.70737	0.70738	0.00003
9864cb1-ttn-um-großen-rutil-P-mill	3 core	NH-11-21	Titanite	1.14	50.9	0.0646	0.70758	0.00005	0.70736	0.70739	0.00005
9864cb1-chip-end-trench2	5 core	NH-11-6	Titanite	0.21	105.7	0.0057	0.70712	0.00003	0.70710	0.70710	0.00003
9864-T8-1	5 core	NH-11-40	Titanite	0.49	125.6	0.0113	0.70709	0.00001	0.70705	0.70706	0.00001
			Rim								
tit-rose	1 rim	NH-47	Titanite	2.59	350.2	0.0214	0.70668	0.00001	0.70661	0.70662	0.00001
9864cb1-area1(spot1-62)	3 rim	NH-11-4	Titanite	0.47	25.4	0.0541	0.70674	0.00007	0.70656	0.70658	0.00007
9864cb1-qtz-albit-line2to4	7 rim	NH-11-26	Quartz-albite	0.12	172.9	0.0020	0.70615	0.00005	0.70614	0.70614	0.00005
9864cb1-ttn-trench2	2 rim	NH-11-27	Titanite	0.65	245.5	0.0077	0.70608	0.00002	0.70605	0.70606	0.00002
cal/alb	2 rim	NH-48	Albite	2.18	20.6	0.3060	0.70694	0.00003	0.70591	0.70602	0.00004
cal/alb	1 rim	NH-49	Albite	2.32	19.2	0.3504	0.70711	0.00006	0.70593	0.70606	0.00007
tit rekristall	2 rim	NH-50	Titanite	2.46	407.0	0.0175	0.70571	0.00001	0.70565	0.70566	0.00001
9864cb1-cc1-P-mill	6 rim	NH-11-13	Calcite	1.86	518.8	0.0103	0.70542	0.00003	0.70539	0.70539	0.00003
9864-calcit-aus-T9	6 rim	NH-11-43	Calcite	0.42	1049	0.0012	0.70563	0.00001	0.70563	0.70563	0.00001
tit-8 rim	1 rim	NH-52	Titanite	0.90	1050	0.0025	0.70538	0.00001	0.70537	0.70537	0.00001
cal-10	2 rim	NH-45	Calcite	0.36	1556	0.0007	0.70533	0.00001	0.70533	0.70533	0.00001
			Matrix								
9864-titanit-incl-rt-matrix	6 matrix	NH-11-31	Titanite	7.91	89.6	0.2555	0.70550	0.00001	0.70464	0.70473	0.00002
9864-titanit-matrix	7 matrix	NH-11-32	Titanite	4.04	178.6	0.0654	0.70472	0.00001	0.70450	0.70452	0.00001
9864-14-2(epi-omph)-matrix	4 matrix	NH-11-39	Amphibole	6.28	92.7	0.1960	0.70534	0.00015	0.70468	0.70475	0.00016
9864-cc-matrix-1	4 matrix	NH-11-29	Calcite	0.14	1346	0.0003	0.70445	0.00001	0.70445	0.70445	0.00001
9864-cc-matrix-1	1 matrix	NH-29	Calcite	0.14	1346	0.0003	0.70445	0.00001	0.70445	0.70445	0.00001
9864-cc-matrix-6	3 matrix	NH-11-38	Calcite	0.17	1456	0.0003	0.70449	0.00001	0.70449	0.70449	0.00001
9864-czoisit-matrix	2 matrix	NH-11-34	Clinozoisite	1.37	2780 [b]	0.0014	0.70467	0.00001	0.70467	0.70467	0.00001
			Vein / Grain bounderies								
9864cb1-cc7-vein-P-mill	2 vein	NH-11-19	Calcite	8.44	298.6	0.0817	0.70804	0.00009	0.70777	0.70780	0.00009
9864-epidot-matrix	1 vein	NH-11-33	Allanite	4.97	5773	0.0025	0.70875	0.00001	0.70874	0.70874	0.00001
T9-aln	1 vein	NH-44	Allanite	0.29	4765	0.0002	0.70855	0.00001	0.70855	0.70855	0.00001

[a] Concentrations were determined by isotope dilution and mixed ^{87}Rb-^{84}Sr tracers.

[b] Concentration was determined by microprobe analysis. [c] Calculated to 240/214 Ma using decay constant recommanded by Villa et al. (2015)

Table 2. Overview of successive fluid-mineral interaction stages, Sr isotope compositions and chemical compositions of titanite I-III.

Fluid-interaction	**Titanite reaction**	**$^{87}Sr/^{86}Sr$ of titanite**	**Chemical characteristics**
episode A Interaction with aqueous internally derived fluid	growth of titanite I in vein	c. 0.7071-0.7076 marble protholith Sr	ttn core XAl=0.18-0.19
episode B Interaction with aqueous fluid	titanite→rutile		Change of XCO_2 and/or P increase
episode C infiltration with mantle derived fluid	back-reaction rutile→titanite II	c.0.7052- 0.7055 mix of Sr from precursor (titanite I) and fluid	high XAl=0.21-0.27 high fluorine content of the fluid is indicated by F- phases apatite, fluorite in the reaction rim
episode D new pulse of interaction with mantle fluid	titanite II→titanite III	c. 0.7045 (in matrix titanite III)	low XAl=0.09-0.15) pervasive dissolution precipitation of matrix minerals calcite, clinozoisite, titanite III
episode E Infiltration with crustal fluid	titanite I→allanite	c. 0.7080 (allanite)	high REE, Th, precipitation of sulfides (Fe, Pb, Cu, Sb) in veins and calcite pores

Supplement S1. Mineral assemblages related to the successive epidodes.

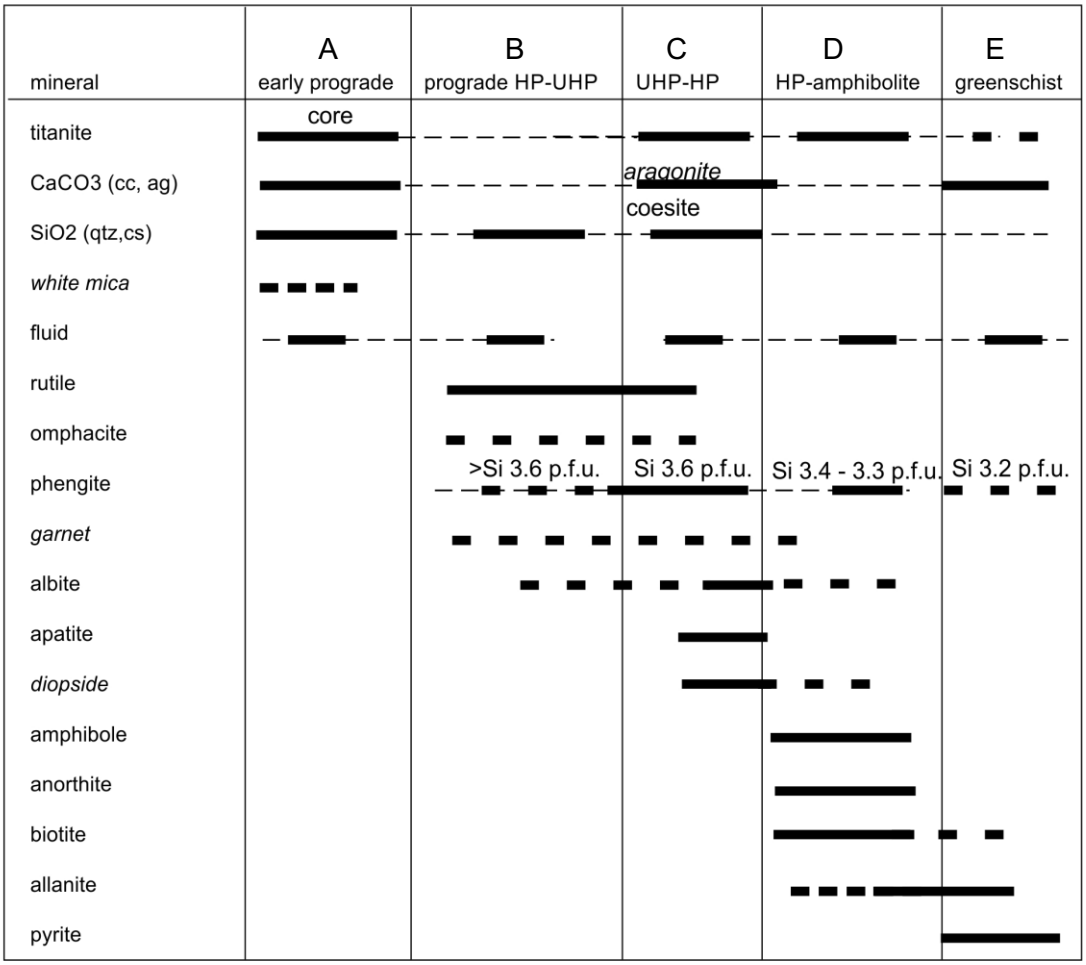

Supplement 2. Chemical compositions of titanite core, reaction rim, and matrix titanite

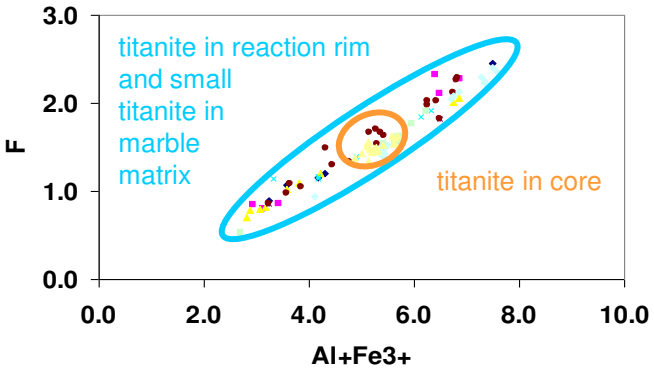

Supplement S3.

Distribution map of Al
from the titanite reaction rim, showing
two reaction fronts (titanite II and III)
with straight boundaries (arrows),
replacing titanite I.
Warm colors relate to high, cold colors to
low Al concentration, resp.

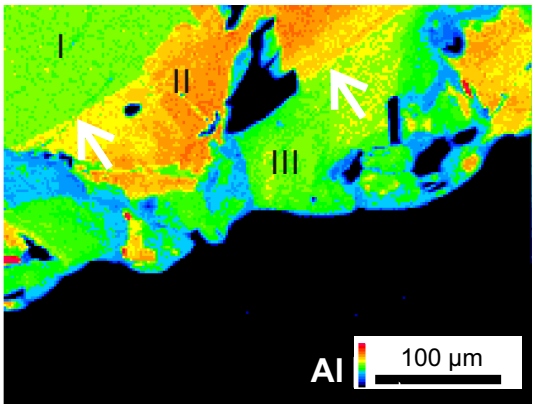

S4. Representative chemical composition of titanite I, II, III. Analyses in wt%. Mineral formulae calculated according to Franz and Spear (1985).

	Titanite I				**Titanite II**				**Titanite III**				
	core	core	core	core	core	rim	rim	rim	rim	matrix	rim	rim	rim
SiO_2	31.22	31.23	31.15	31.36	31.08	31.60	31.33	31.55	31.58	31.22	31.14	30.94	31.20
TiO_2	33.47	33.35	32.71	32.93	33.13	31.85	30.48	30.33	31.06	34.82	37.26	37.52	35.67
Al_2O_3	4.93	4.88	5.08	5.09	5.10	5.95	6.96	6.99	6.57	3.65	2.40	2.20	3.37
Fe_2O_3	0.49	0.47	0.56	0.51	0.55	0.27	0.22	0.30	0.27	0.46	0.31	0.31	0.36
MnO	0.04	0.08	0.02	0.02	0.03	0.00	0.03	0.00	0.02	0.02	0.00	0.02	0.02
CaO	28.72	28.79	28.72	28.48	28.70	29.10	29.20	28.96	28.86	29.17	28.72	29.08	28.94
Na_2O	0.09	0.08	0.11	0.07	0.07	0.05	0.05	0.04	0.07	0.02	0.02	0.00	0.06
F	1.48	1.51	1.54	1.50	1.53	1.91	2.14	2.30	2.13	0.94	0.52	0.44	0.87
sum	100.43	100.39	99.88	99.97	100.19	100.73	100.42	100.47	100.56	100.28	100.37	100.50	100.49
Al+Fe3+	0.20	0.20	0.21	0.21	0.21	0.23	0.27	0.27	0.25	0.15	0.10	0.09	0.14
Ti	0.81	0.80	0.79	0.80	0.80	0.76	0.73	0.73	0.75	0.84	0.90	0.91	0.86
F	0.15	0.15	0.16	0.15	0.16	0.19	0.22	0.23	0.22	0.10	0.05	0.04	0.09
X(Al)	0.19	0.18	0.19	0.19	0.19	0.23	0.26	0.26	0.25	0.14	0.09	0.08	0.13

(Al 3+ + Fe 3+) = (OH- + F-)
after Enami, M., Suzuki, K., Liou, J. G., Bird, D. K., 1993. Al-Fe3+ and F-OH substitutions in titanite and constraints on their PT dependence. European Journal of Mineralogy, 219-232.
X(Al) = Al/(Al + Ti + Fe3+)
after Oberti, R., Smith, D.C., Rossi, G., Caucia, F., 1981. The crystal-chemistry of high-aluminium titanites. *European Journal of Mineralogy* , pp.777-792.

Representative chemical composition of carbonate from marble matrix, reaction rim and veins. Analyses in wt%.

Comment	SiO_2	Al_2O_3	TiO_2	CaO	BaO	MgO	FeO	MnO	CO_2	Total
Carb-9864	0.39	0.00	0.00	31.40	0.00	13.86	7.32	0.09	46.93	99.99
Carb-9864	0.13	0.00	0.02	37.75	0.00	10.49	6.27	0.10	45.24	100.01
Carb-9864	0.02	0.00	0.01	31.79	0.00	13.49	7.70	0.13	46.87	100.00
Carb-9864	0.02	0.00	0.00	54.04	0.02	0.97	0.97	0.07	43.92	100.00
Carb-9864	0.05	0.00	0.00	54.17	0.03	0.86	0.90	0.06	43.94	100.00
Carb-9864	0.01	0.00	0.00	54.00	0.00	0.75	0.78	0.04	44.42	100.00
Carb-9864	0.02	0.00	0.00	54.50	0.02	0.66	0.70	0.06	44.04	100.01
Carb-9864	0.00	0.00	0.00	54.01	0.03	0.82	0.79	0.04	44.31	100.00
Carb-9864	0.01	0.00	0.05	55.77	0.02	0.14	0.28	0.16	43.57	99.99
Carb-9864	0.00	0.00	0.01	55.28	0.03	0.19	0.41	0.15	43.91	100.00
Carb-9864	0.00	0.00	0.00	55.42	0.00	0.17	0.31	0.17	43.93	100.01
Carb-9864	0.00	0.01	0.00	54.08	0.03	0.65	1.16	0.20	43.86	99.99
Carb-9864	0.03	0.00	0.02	54.18	0.00	0.61	1.12	0.19	43.84	100.00
Carb-9864	0.20	0.03	0.23	54.31	0.01	0.61	1.06	0.20	43.35	99.99
Carb-9864	0.01	0.00	0.00	54.29	0.00	0.74	1.09	0.15	43.72	100.00
Carb-9864	0.02	0.00	0.04	57.61	0.00	0.02	0.01	0.04	42.27	100.00
Carb-9864	0.02	0.00	0.00	57.43	0.03	0.00	0.03	0.00	42.49	100.00
Carb-9864	0.21	0.00	0.05	56.74	0.00	0.01	0.02	0.02	42.95	100.00
Carb-9864	0.00	0.00	0.02	57.00	0.03	0.00	0.04	0.02	42.89	100.00
Carb-9864	0.03	0.00	0.01	57.31	0.02	0.00	0.14	0.03	42.47	100.01
Carb-9864	0.01	0.01	0.03	57.16	0.01	0.00	0.00	0.09	42.70	100.00